

## Low-Frequency Dynamic Ocean Response to Barometric-Pressure Loading

CHRISTOPHER G. PIECUCH,<sup>a</sup> ICHIRO FUKUMORI,<sup>b</sup> RUI M. PONTE,<sup>c</sup> MICHAEL SCHINDELEGGER,<sup>d</sup> OU WANG,<sup>b</sup>  
AND MENGAN ZHAO<sup>c</sup>

<sup>a</sup> Woods Hole Oceanographic Institution, Woods Hole, Massachusetts

<sup>b</sup> Jet Propulsion Laboratory, California Institute of Technology, Pasadena, California

<sup>c</sup> Atmospheric and Environmental Research, Inc., Lexington, Massachusetts

<sup>d</sup> Universität Bonn, Bonn, Germany

(Manuscript received 19 April 2022, in final form 27 June 2022)

**ABSTRACT:** Changes in dynamic manometric sea level  $\zeta_m$  represent mass-related sea level changes associated with ocean circulation and climate. We use twin model experiments to quantify magnitudes and spatiotemporal scales of  $\zeta_m$  variability caused by barometric pressure  $p_a$  loading at long periods ( $\geq 1$  month) and large scales ( $\geq 300$  km) relevant to Gravity Recovery and Climate Experiment (GRACE) ocean data. Loading by  $p_a$  drives basin-scale monthly  $\zeta_m$  variability with magnitudes as large as a few centimeters. Largest  $\zeta_m$  signals occur over abyssal plains, on the shelf, and in marginal seas. Correlation patterns of modeled  $\zeta_m$  are determined by continental coasts and  $H/f$  contours ( $H$  is ocean depth and  $f$  is Coriolis parameter). On average,  $\zeta_m$  signals forced by  $p_a$  represent departures of  $\leq 10\%$  and  $\leq 1\%$  from the inverted-barometer effect  $\zeta^{\text{ib}}$  on monthly and annual periods, respectively. Basic magnitudes, spatial patterns, and spectral behaviors of  $\zeta_m$  from the model are consistent with scaling arguments from barotropic potential vorticity conservation. We also compare  $\zeta_m$  from the model driven by  $p_a$  to  $\zeta_m$  from GRACE observations. Modeled and observed  $\zeta_m$  are significantly correlated across parts of the tropical and extratropical oceans, on shelf and slope regions, and in marginal seas. Ratios of modeled to observed  $\zeta_m$  magnitudes are as large as  $\sim 0.2$  (largest in the Arctic Ocean) and qualitatively agree with analytical theory for the gain of the transfer function between  $\zeta_m$  forced by  $p_a$  and wind stress. Results demonstrate that  $p_a$  loading is a secondary but nevertheless important contributor to monthly mass variability from GRACE over the ocean.

**KEYWORDS:** Barotropic flows; Large-scale motions; Ocean circulation; Planetary waves; Potential vorticity; Sea level

### 1. Introduction

Understanding the ocean's response to forcing by the atmosphere has been a longstanding goal in ocean physics (Gill and Niiler 1973; Magaard 1977; Philander 1978; Willebrand et al. 1980; Frankignoul et al. 1997). There is a rich literature on the oceanic response to barometric pressure  $p_a$  forcing (Brown et al. 1975; Close 1918; Doodson 1924; Ponte 1992; Proudman 1929; Wunsch and Stammer 1997). Surface loading by  $p_a$  is generally thought to drive an isostatic ocean response, which is described in terms of sea level  $\zeta$  by the inverted-barometer (IB) effect


$$\zeta^{\text{ib}} = -\frac{p_a - \bar{p}_a}{\rho_0 g}, \quad (1)$$

where  $\rho_0$  is surface density,  $g$  is gravitational acceleration, and overbar is global ocean average. Altimetry largely corroborates an IB paradigm (Fu and Pihos 1994; Gaspar and Ponte 1997; Ponte and Gaspar 1999; vanDam and Wahr 1993; Wunsch 1991). Under a perfect IB response,  $\zeta$  changes compensate the surface load, subsurface density and pressure

gradients are unchanged, and ocean currents are largely unaffected. Since ocean circulation is mostly unperturbed in the IB scenario,  $p_a$  is often omitted from the surface boundary conditions used in data-constrained global ocean state estimates and reanalyses (Ferry et al. 2012; Forget et al. 2015; Köhl 2015; Storto et al. 2016).

While it provides a useful approximation, the IB assumption seldom holds strictly. How accurately the IB effect describes the ocean's response to  $p_a$  depends on frequency, wavenumber, and location (Wunsch and Stammer 1997). At short periods of days to weeks and on subbasin scales, the IB assumption breaks down, and prominent dynamic  $\zeta$  responses to  $p_a$  occur from wave adjustments and basin modes as well as frictional effects on the shelf and in marginal seas (Greatbatch et al. 1996; Hirose et al. 2001; Mathers and Woodworth 2001; Ponte 1993, 1994, 1997; Ponte et al. 1991; Tierney et al. 2000; Wright et al. 1987). Such deviations from isostasy are well known, and partly motivate the use of models driven by  $p_a$  and winds to simulate  $<20$ -day nonequilibrium signals for dealiasing satellite-altimetry  $\zeta$  data (Carrère and Lyard 2003; Carrère et al. 2016).

Even excluding high-frequency resonant responses and frictional effects over shallow bathymetry, a purely isostatic response to  $p_a$  forcing is generally not expected (Brown et al. 1975; Ponte et al. 1991). When interrogating such departures from isostasy, it is instructive to consider dynamic manometric sea level (see appendix A for a discussion of this quantity)

 Denotes content that is immediately available upon publication as open access.

Corresponding author: Christopher G. Piecuch, cpiecuch@whoi.edu

DOI: 10.1175/JPO-D-22-0090.1

© 2022 American Meteorological Society. For information regarding reuse of this content and general copyright information, consult the AMS Copyright Policy (www.ametsoc.org/PUBSReuseLicenses).

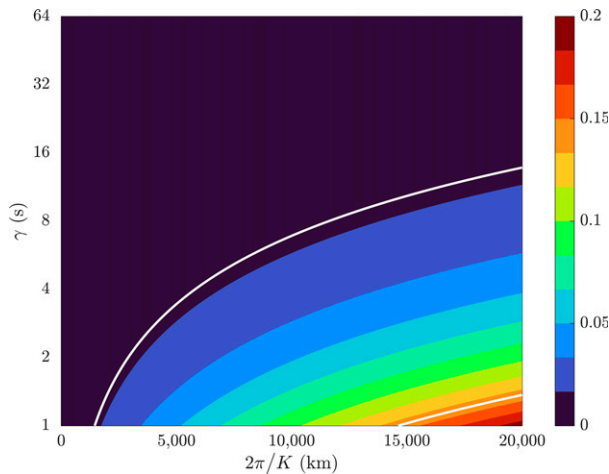


FIG. 1. Values of the transfer function  $h = \omega/gK\gamma$  for variable  $K$  and  $\gamma$  (4). Values are averaged over frequencies between  $\omega = 0$  and  $\omega = 2\pi/2$  months (the Nyquist angular frequency of GRACE and GRACE-FO). White contours identify values of 0.01 and 0.14, which are the 0.5th and 99.5th percentiles of values in Fig. 5.

$$\zeta_m = \frac{p_b - \bar{p}_a}{\rho_0 g}, \quad (2)$$

where  $p_b$  is ocean bottom pressure. Changes in  $\zeta_m$  identify  $\zeta$  changes from mass changes relevant to ocean circulation and climate. No  $\zeta_m$  changes occur for an IB response (Ponte et al. 2007). Consideration of  $\zeta_m$  may thus inform interpretation of Gravity Recovery and Climate Experiment (GRACE) and GRACE Follow-On (FO) ocean data (Landerer et al. 2020; Tapley et al. 2019).

Some rough orders of magnitude are instructive. For a linear, inviscid, barotropic ocean forced by  $p_a$  at long periods ( $\geq 1$  month) and large scales ( $\geq 300$  km) relevant to GRACE, potential vorticity conservation is written in terms of  $\zeta_m$  as (see appendix B for a derivation)

$$g\mathbf{J}\left(\zeta_m, \frac{H}{f}\right) = -\frac{\partial \zeta^{\text{ib}}}{\partial t}, \quad (3)$$

where  $\mathbf{J}$  is Jacobian determinant,  $H$  is ocean depth,  $f$  is Coriolis parameter, and  $t$  is time. The balance in (3) is between forcing displacement and motion across  $H/f$  contours, analogous to a Sverdrup balance—the changing load stretches or squashes the water column similar to Ekman pumping by wind stress curl (Gill 1982). While the forcing displacement on the right side of (3) is written in terms of  $\zeta^{\text{ib}}$  for convenience,  $\zeta_m$  is driven causally by the variable surface load, not the ocean's isostatic response per se. According to (3), the admittance (or transfer) function between  $\zeta_m$  and  $\zeta^{\text{ib}}$  is (appendix B)

$$h(\zeta_m, \zeta^{\text{ib}}) = \frac{\mathcal{F}(\zeta_m)}{\mathcal{F}(\zeta^{\text{ib}})} = \frac{\omega}{gK\gamma}, \quad (4)$$

where  $\mathcal{F}$  is Fourier transform,  $\omega$  is angular frequency,  $K$  is the projection of the wavenumber vector along  $H/f$  contours, and

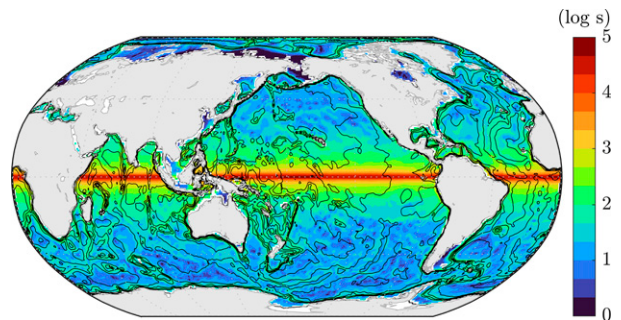


FIG. 2. Color shading indicates values of  $\gamma$  (the magnitude of the  $H/f$  gradient). Units are seconds. Note the logarithmic color scale. Black contours indicate  $H$  contours between 0 and 6000 m at 1000-m increments.

$\gamma$  is the magnitude of the  $H/f$  gradient. From (4), we see that magnitudes of  $\zeta_m$  variations relative to  $\zeta^{\text{ib}}$  fluctuations increase with higher frequencies, larger scales, and weaker  $H/f$  gradients. Depending on  $K$  and  $\gamma$ , (4) predicts that monthly  $\zeta_m$  signals can be as large as 10% of  $\zeta^{\text{ib}}$  fluctuations (Fig. 1). For example, variations of  $\zeta^{\text{ib}} \sim 5$  cm over abyssal plains where  $\gamma \geq 2$  s (Fig. 2) translate to fluctuations of  $\zeta_m \lesssim 5$  mm. Such signals are not negligible relative to variability from GRACE (Quinn and Ponte 2012), hinting that such effects may indeed be relevant for interpreting satellite-gravimetric mass data over the ocean. Revisiting departures from isostasy may be timely more generally given the increasing use of models for assimilating ocean observations (Heimbach et al. 2019).

Thus, while the dynamic  $\zeta$  response to  $p_a$  has been studied using altimetry or numerical models with an emphasis on weekly and shorter periods, it remains to probe monthly and longer periods in the context of  $\zeta_m$  and gravimetry. As part of recent Estimating the Circulation and Climate of the Ocean (ECCO) efforts (Fukumori et al. 2021), we started including  $p_a$  as one of the boundary conditions to force a general circulation model for ocean state estimation. This effort offers a timely opportunity to revisit the ocean's dynamic response to  $p_a$  loading. Here we interrogate twin model experiments to quantify magnitudes and spatiotemporal scales of the  $\zeta_m$  response to  $p_a$  loading, and establish the relevance for interpreting satellite-gravity mass data over the ocean.

## 2. Methods

### a. ECCO state estimate

We use the latest (Release 4) ocean state estimate from the ECCO Version 4 nonlinear inverse modeling framework. The solution and approach are detailed elsewhere (Forget et al. 2015; Fukumori et al. 2021; Wunsch and Heimbach 2013), but we give a short description for completeness. The estimate is a solution to a Boussinesq general circulation model (Marshall et al. 1997) constrained to modern ocean observations (e.g., altimetry, GRACE, Argo) through an iterative procedure that preserves physical consistency—initial conditions, boundary conditions, and mixing coefficients are adjusted within acceptable bounds until agreement between model and

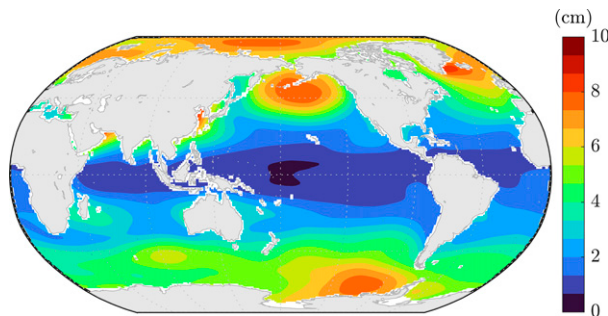


FIG. 3. Color shading indicates values of  $\sigma_{\zeta^{\text{ib}}}$  (the standard deviation of the IB effect). Units are centimeters. Values are based on monthly model output during 1993–2017.

data is sufficiently good (Heimbach et al. 2005; Wunsch and Heimbach 2007).

Release 4 is an update to earlier ECCO Version 4 state estimates (Forget et al. 2015, 2016; Fukumori et al. 2017). It spans 1992–2017 and covers the global ocean. The spatial grid has  $\sim 1^\circ$  horizontal resolution and 50 vertical levels with variable thickness from 10 m near the surface to  $\sim 460$  m at depth. Partial cells are used to represent topography. Unresolved small-scale effects are parameterized (Redi 1982; Gent and McWilliams 1990; Gaspar et al. 1990). Surface forcing is based on atmospheric variables from a reanalysis (Dee et al. 2011), some of which are adjusted as part of the estimation. Results here are based on detrended monthly output over 1993–2017.

Unlike past ECCO Version 4 solutions, Release 4 includes 6-hourly  $p_a$  in the surface boundary conditions. Periodic  $p_a$  signals from diurnal and semidiurnal atmospheric tides are removed prior to the simulations. Otherwise, no adjustments are made to this forcing. As context for results below, the  $p_a$  forcing is summarized in Fig. 3 in the form of standard deviations  $\sigma$  of monthly  $\zeta^{\text{ib}}$  values. Similar maps are published elsewhere (Ponte 2006, their Fig. 2). Values show clear large-scale spatial structure, increasing from  $\sigma_{\zeta^{\text{ib}}} \lesssim 1$  cm at low latitudes to  $\sigma_{\zeta^{\text{ib}}} \gtrsim 5$  cm at high latitudes. Enhanced variability  $\sigma_{\zeta^{\text{ib}}} \gtrsim 7$  cm appears over the Pacific sector of the Southern Ocean, extratropical North Pacific Ocean, Yellow Sea, Persian Gulf, Nordic seas, and Arctic Ocean. These regional  $\zeta^{\text{ib}}$  features likely identify variations in semipermanent  $p_a$  centers (e.g., Aleutian low, Icelandic low) or the East Asian monsoon. Given (1), since  $\bar{p}_a$  contributions to  $\zeta^{\text{ib}}$  are small and relatively unimportant outside the tropics<sup>1</sup> (Wunsch and Stammer 1997; Ponte 2006), Fig. 3 can be qualitatively interpreted in terms of local  $p_a$  variability, with an increase in  $\zeta^{\text{ib}}$  of 1 cm equating to a drop in  $p_a$  of  $\sim 1$  hPa.

We use twin model simulations to quantify the  $\zeta_m$  response to  $p_a$  forcing. The first simulation is the ECCO Version 4 Release 4 solution itself, which includes variable  $p_a$  loading among the surface boundary conditions. The second simulation is nearly identical to the first, only now the model omits  $p_a$  forcing. In all other respects, the two simulations are the

same. We isolate  $\zeta_m$  changes caused by  $p_a$  loading by differencing the two solutions under the assumption of a linear response.<sup>2</sup> All modeled results in the text are based on differences taken between simulations.

### b. GRACE satellite gravimetry

We also use GRACE ocean data (Tapley et al. 2019). These data reflect changes in the local mass of the water–ice–air column above the seafloor. Fields covering the time period from April 2002 to May 2021 were downloaded from the GRACE Tellus website hosted by the National Aeronautics and Space Administration Jet Propulsion Laboratory on 25 August 2021 (data version GRCTellus.JPL.200204\_202105.GLO.RL06M.MSCNV02CRI). Data are defined based on  $3^\circ$  spherical-cap mass-concentration-block gravity-field basis functions and given on a  $0.5^\circ$  global spatial grid. Note that GRACE does not resolve surface mass redistribution on spatial scales  $\lesssim 300$  km. Fields are given in terms of the quantity  $p_b/\rho_0g$  and have equivalent water thickness units. See Watkins et al. (2015) and Wiese et al. (2016) for technical details on the GRACE estimation process (spatial constraints, scale factors, leakage errors, coastline resolution, etc.). To compute  $\zeta_m$  from GRACE retrievals, we subtract a time series of  $\bar{p}_a/\rho_0g$  from the mass data at each ocean grid cell after Eq. (2) using  $\bar{p}_a$  from reanalysis provided by GRACE Tellus.

For purposes of comparison, we make some adjustments to the ECCO and GRACE  $\zeta_m$  fields. To focus on dynamics, we remove from GRACE  $\zeta_m$  data at each ocean grid cell the time series of  $\bar{\zeta}_m$  related to changes in global ocean mass from freshwater fluxes between the ocean and other elements of the climate system. No such adjustment is made for ECCO because, given the design of the experiments, modeled  $\zeta_m$  values arise almost entirely from redistribution of mass in the ocean—effects of surface freshwater flux included in the model forcing largely cancel out between the two experiments. We also interpolate the ECCO solutions onto the GRACE space–time intervals. For each monthly average, we bilinearly interpolate the ECCO solution from its  $\sim 1^\circ$  native grid onto the GRACE  $0.5^\circ$  global grid, and for each grid cell, we linearly interpolate monthly  $\zeta_m$  from ECCO onto the increments of the GRACE data, which are gappy and have nominal monthly frequency, over the common period between April 2002 and June 2017. Finally, we remove local linear temporal trends from GRACE at each grid cell.

## 3. Results

### a. Magnitudes

Magnitudes of  $\zeta_m$  signals forced by  $p_a$  vary by an order of magnitude over the ocean (Fig. 4a). Typical  $\sigma_{\zeta_m}$  values are on the order  $\sim 1$  mm. Larger values appear in semienclosed marginal seas

<sup>1</sup> The time series of  $\bar{p}_a$  is dominated by the seasonal cycle, which has an amplitude  $\sim 1$  hPa (e.g., Fig. 3a in Wunsch and Stammer 1997).

<sup>2</sup> Strictly speaking, since the model is forced by bulk formulas, differences may exist between the two simulations in terms of surface heat and freshwater fluxes, which may influence our results. However, since we anticipate a mostly linear response, and because model results are consistent with basic considerations from  $p_a$ -forced ocean dynamics (see below), we assume that such nonlinear effects have a small effect and do not pursue them further.

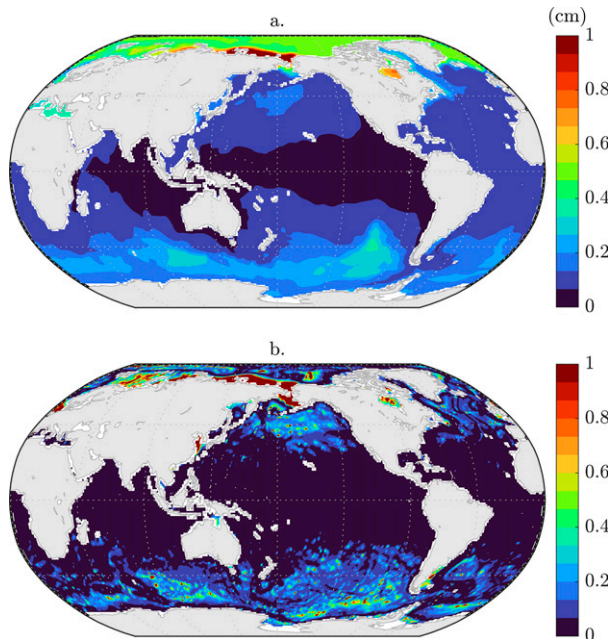


FIG. 4. (a) Color shading indicates values of  $\sigma_{\zeta_m}$  (the standard deviation of manometric sea level). Units are centimeters. Values are based on monthly model output during 1993–2017. (b) Color shading indicates ratios of  $\sigma_{\zeta^{ib}}$  to  $\gamma$  (Fig. 3 divided by Fig. 2). We set  $\min(\gamma) = 1$  s to avoid overly large values of  $\sigma_{\zeta^{ib}}/\gamma$ . Values are scaled, and units are arbitrary.

including the Arctic Ocean, Hudson Bay, and the Mediterranean Sea, on broad shelf regions including the Scotian and Patagonian Shelves, and over deep midlatitude abyssal plains including the Amundsen–Bellingshausen, Australian–Antarctic, Weddell–Enderby, and Pacific Basins. Especially noteworthy are signals  $\sigma_{\zeta_m} \geq 1$  cm evident along the Kara, Laptev, East Siberian, and Bering Seas on the continental shelf of the Russian sector of the Arctic Ocean. In contrast,  $\zeta_m$  behavior is more muted in the tropics and on the equator. Qualitative similarities are observed between Figs. 3 and 4a (e.g., both display values that generally increase from low to high latitude), but the spatial patterns of  $\sigma_{\zeta^{ib}}$  and  $\sigma_{\zeta_m}$  feature important differences that suggest the role of dynamical mechanisms in mediating the ocean’s response to  $p_a$  forcing.

Variations in  $\zeta_m$  are one or two orders of magnitude smaller than  $\zeta^{ib}$  fluctuations (Fig. 5). By comparing  $\sigma_{\zeta_m}$  to  $\sigma_{\zeta^{ib}}$ , we quantify the fractional deviation from isostasy. Ratios of  $\sigma_{\zeta_m}$  to  $\sigma_{\zeta^{ib}}$  can be relatively small  $\leq 0.02$  in regions where  $\sigma_{\zeta^{ib}}$  values are the largest, such as the Arabian Sea, Bay of Bengal, Yellow Sea, northeast Pacific Ocean along the Aleutian Islands, and northeast Atlantic Ocean. Comparatively large values  $\sigma_{\zeta_m}/\sigma_{\zeta^{ib}} \geq 0.05$  are apparent along the equator, where  $\sigma_{\zeta^{ib}}$  values are particularly small, as well as across parts of the Amundsen–Bellingshausen, Australian–Antarctic, Weddell–Enderby, and Argentine Basins, on the American continental shelf, in Hudson Bay and the Mediterranean Sea, and broadly over the Nordic seas and Arctic Ocean, most notably along the East Siberian and Laptev Seas, where  $\sigma_{\zeta_m}$  values are the largest.

Ratios of  $\sigma_{\zeta_m}$  to  $\sigma_{\zeta^{ib}}$  determined from the model are qualitatively consistent with expectations from basic theory. Ninety-nine

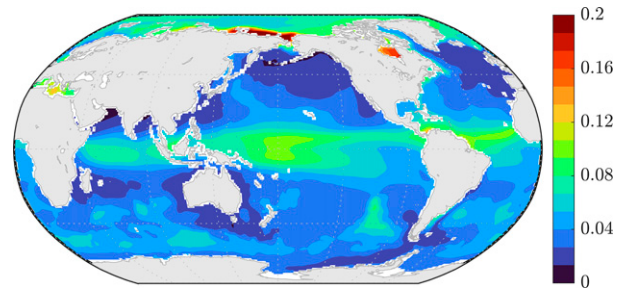


FIG. 5. Color shading indicates ratios of  $\sigma_{\zeta_m}$  to  $\sigma_{\zeta^{ib}}$  (Fig. 4a divided by Fig. 3).

percent of the values shown in Fig. 5 are between 0.01 and 0.14. A similar range is anticipated from (4) for  $2\pi/K \sim 1000$ – $20000$  km and  $\gamma \sim 1$ – $10$  s (Fig. 1). Using the quasigeostrophic theory developed by Brown et al. (1975), Ponte et al. (1991) report similar deviations from isostasy on the order of a few percent at monthly periods (their Table 1). But, since their theory applies to a flat-bottom midlatitude  $\beta$ -plane ocean, they do not predict the larger deviations that we observe at higher and lower latitudes, on the shelf, and in marginal seas.

The rough agreement between model and theory (Figs. 1, 5) does not establish that (3) fully describes the physics responsible for the detailed  $\sigma_{\zeta_m}/\sigma_{\zeta^{ib}}$  patterns. To test the ability of (3) to predict the modeled  $\sigma_{\zeta_m}$  spatial structure (Fig. 4a), we consider patterns of  $\sigma_{\zeta^{ib}}/\gamma$  (Fig. 4b). Ratios of  $\sigma_{\zeta^{ib}}$  to  $\gamma$  can be interpreted in terms of the low-frequency, large-scale  $\zeta_m$  response to local  $p_a$  at fixed frequency and wavenumber (3) and (4). Patterns of  $\sigma_{\zeta^{ib}}/\gamma$  reproduce some qualitative features of the  $\sigma_{\zeta_m}$  structure, including elevated values over abyssal plains, marginal seas, and shelf regions identified earlier. The correlation coefficient between Figs. 4a and 4b is  $\sim 0.6$ , suggesting that the physics embodied by (3) and local  $p_a$  indeed explain some of the spatial variance in  $\sigma_{\zeta_m}$  patterns. However, there are clear differences between the two maps. For example, the  $\sigma_{\zeta^{ib}}/\gamma$  pattern is less smooth and shows more small-scale noise than the  $\sigma_{\zeta_m}$  structure. These differences may implicate remote effects, such as free motions along  $H/f$  contours.

#### b. Horizontal scales

To quantify the dominant horizontal scales of  $\zeta_m$  variability, we compute the cross-correlation matrix between all pairs of  $\zeta_m$  time series over the ocean. This provides a test of our anticipation that  $\zeta_m$  signals due to  $p_a$  have large spatial scales. Instances are provided in Fig. 6, which shows global maps of correlation coefficients between  $\zeta_m$  time series from six example locations and  $\zeta_m$  everywhere else. These example locations were chosen from the different basins, including ones with relatively strong  $\sigma_{\zeta_m}$  values in the Arctic, Southern, and extratropical North Pacific Oceans, as well as ones with comparatively weak  $\sigma_{\zeta_m}$  values in the western equatorial Pacific and Atlantic Oceans (cf. Fig. 4a). For reference, given time series with 300 degrees of freedom, correlation coefficients with magnitudes  $\geq 0.17$  are distinguishable from zero at the 99% confidence level.

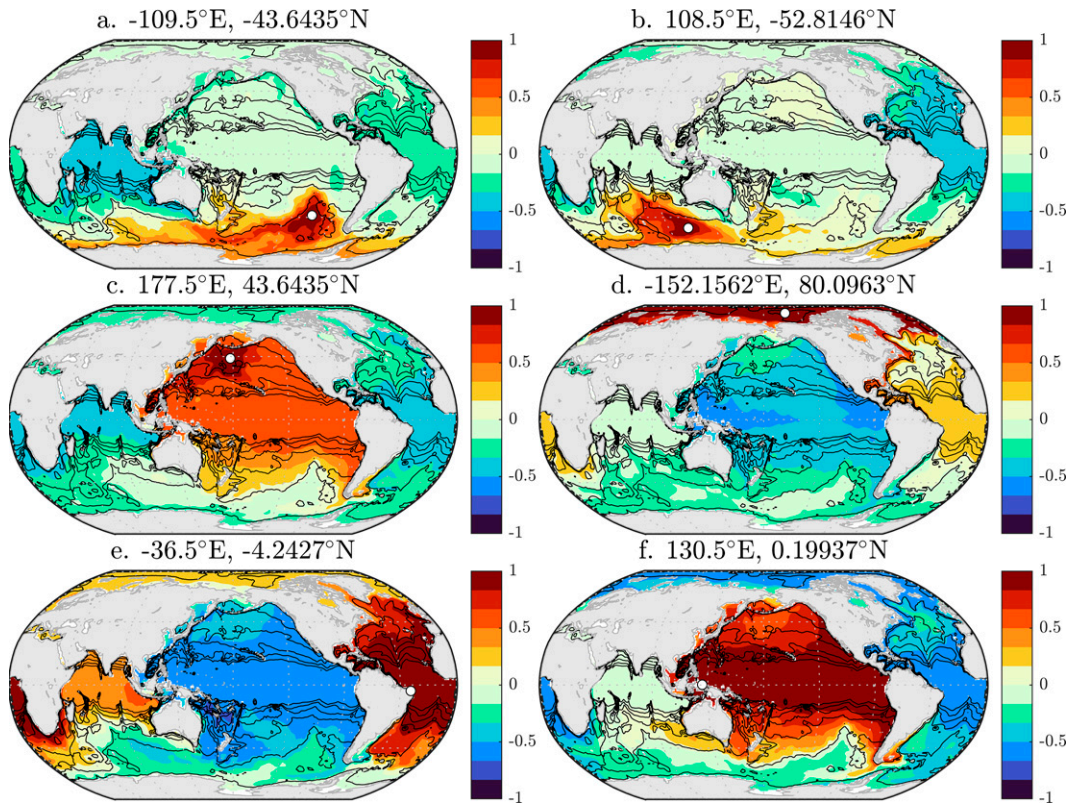


FIG. 6. Color shading indicates correlation coefficients between  $\zeta_m$  over the global ocean and  $\zeta_m$  in the (a) Amundsen–Bellinghousen Basin, (b) Australian–Antarctic Basin, (c) extratropical North Pacific Ocean, (d) Beaufort Sea, (e) western equatorial Atlantic Ocean, and (f) western equatorial Pacific Ocean (see white circles in the various panels). Lightly shaded values have magnitudes  $\leq 0.17$  and are not distinguishable from zero at the 99% confidence level. Black contours indicate  $H/f$  contours between  $2 \times 10^7$  and  $12 \times 10^7$  m s at increments of  $2 \times 10^7$  m s.

Fluctuations in  $\zeta_m$  covary across basin scales (Fig. 6). For example,  $\zeta_m$  variations over the Amundsen–Bellinghousen and Australian–Antarctic Basins are coherent with  $\zeta_m$  broadly over the Southern Ocean (Figs. 6a,b). We also see that  $\zeta_m$  changes over the extratropical North Pacific Ocean are correlated with  $\zeta_m$  elsewhere over the entire Pacific Ocean, and that  $\zeta_m$  behavior over the Beaufort Sea covaries with  $\zeta_m$  not only across the Arctic Ocean and the Nordic Seas, but also on the shelf and slope of eastern North America and the tropical Atlantic Ocean (Figs. 6c,d). Interrogating low-latitude behavior, we find that  $\zeta_m$  variability in the western equatorial Atlantic Ocean off Brazil is correlated with  $\zeta_m$  over the Atlantic Ocean and, to a lesser extent, Indian and Arctic Oceans, whereas  $\zeta_m$  behavior in the western equatorial Pacific Ocean near Papua exhibits coherence with  $\zeta_m$  across the Pacific Ocean (Figs. 6e,f). These basin-scale  $\zeta_m$  signals imply subtle mass convergences and divergences. For example, a  $\sim 1$ -mm monthly  $\zeta_m$  anomaly over the Pacific Ocean (surface area  $\sim 2 \times 10^{14}$  m<sup>2</sup>) requires a monthly transport anomaly of just  $\sim 0.1$  Sv ( $1 \text{ Sv} \equiv 10^6 \text{ m}^3 \text{ s}^{-1}$ ).

Cross-correlation patterns in Fig. 6 hint at mechanisms that may mediate the  $\zeta_m$  response. Basin-scale regions of coherent  $\zeta_m$  variation are essentially bounded by  $H/f$  contours and coasts, suggesting that barotropic planetary waves are involved in facilitating the transient ocean adjustment process

(Hughes et al. 2019, their Fig. 1). In the Southern Ocean,  $H/f$  contours largely conform to bathymetry, and continental boundaries are absent at the latitudes of Drake Passage. Thus, spatial correlation patterns of  $\zeta_m$  signals there are strongly influenced by the Chile, Pacific Antarctic, Southeast Indian, and Southwest Indian Ridges, which isolate the Australian–Antarctic, Amundsen–Bellinghousen, and Weddell–Enderby Basins from other deep ocean basins.

Correlation patterns elsewhere can be understood in terms of equatorial, coastal, and Rossby wave propagation. Figure 6f gives an instructive example. Equatorial Kelvin waves propagating eastward across the equatorial Pacific Ocean, coastal Kelvin waves progressing poleward in the cyclonic sense along the west coast of the Americas, and Rossby waves radiating westward into the interior from the eastern boundary could explain the enhanced correlations observed between  $\zeta_m$  in the western equatorial Pacific Ocean and  $\zeta_m$  elsewhere over the Pacific Ocean.<sup>3</sup> The abrupt change in correlation between the North Pacific and Arctic Oceans may reflect a

<sup>3</sup> Given the rapid phase speeds of barotropic waves, time scales of the transient adjustment process are generally much shorter than the monthly periods being studied here.

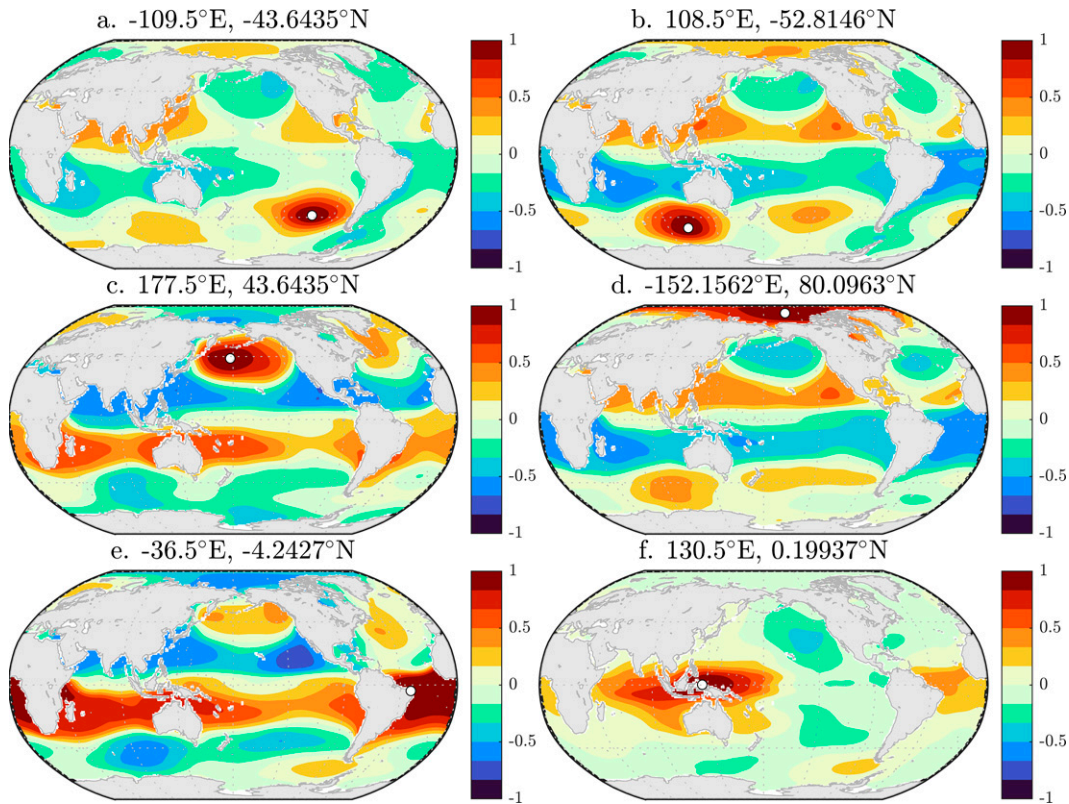


FIG. 7. Color shading indicates correlation coefficients between  $\zeta^{\text{ib}}$  over the global ocean and  $\zeta^{\text{ib}}$  in the (a) Amundsen–Bellinghousen Basin, (b) Australian–Antarctic Basin, (c) extratropical North Pacific Ocean, (d) Beaufort Sea, (e) western equatorial Atlantic Ocean, and (f) western equatorial Pacific Ocean (see white circles in the various panels). Lightly shaded values have magnitudes  $\leq 0.17$  and are not distinguishable from zero at the 99% confidence level.

communication barrier between the two basins related to the shallow depth or narrow width of the Bering Strait relative to relevant barotropic length scales. Signals appear to exit the Pacific Ocean following the coastal waveguide. Elevated correlations persist along Chile, through northern Drake Passage, and across the Patagonia shelf, dissipating downstream off Brazil where the shelf narrows. The southern boundary of the region of coherence seems to be set by  $H/f$  contours rather than by continental coastlines. A correlation gradient exists between the southwest Pacific and Amundsen–Bellinghousen Basins across  $H/f$  contours demarcated by the Pacific Antarctic and Chile Ridges. Importantly, the Chile Ridge intersects the slope off southwestern South America, hinting that the  $H/f$  contours that set the region's southern boundary are the southernmost  $H/f$  contours emanating from around South America along which Rossby waves propagate from the eastern boundary. Similar reasoning can be used to interpret the correlation patterns for signals in other basins (Figs. 6c–e).

The spatial patterns in Fig. 6 also imply interbasin mass exchange. In addition to large-scale regions with positive correlations, there are also broad ocean areas with negative correlations. For example,  $\zeta_m$  in the western equatorial Atlantic Ocean is anticorrelated with  $\zeta_m$  across the Pacific Ocean, and  $\zeta_m$  in the western equatorial Pacific Ocean is in antiphase with  $\zeta_m$  across the Atlantic and Arctic Oceans (Figs. 6e,f). These

correlation patterns are similar to covariance structures reported by Stepanov and Hughes (2006) in their study of basin-scale signal propagation from a barotropic model. They identify a primary exchange between the Southern and Pacific Oceans at intraseasonal periods, which they interpret in terms of circumpolar wind and form stress around Drake Passage. By elucidating these subtle interbasin exchanges and basin modes forced by  $p_a$  at monthly and longer periods, our results thus complement the earlier findings of Stepanov and Hughes (2006), which emphasize the wind-driven ocean response on these time scales. Note that Chambers and Willis (2009) also discuss mass exchange between the Atlantic and Pacific Oceans using monthly GRACE data over 2002–08, but they do not identify the underlying forcing and dynamics.

We also interrogate cross-correlation patterns determined from  $\zeta^{\text{ib}}$  (Fig. 7). Comparing Figs. 6 and 7, we observe that spatial covariance structures typifying the atmospheric forcing and oceanic response are distinct. On the one hand, regions of coherent  $\zeta_m$  variations have larger basin scales, are simply connected (contiguous), and feature more abrupt boundaries determined by  $H/f$  and coastlines. On the other hand, areas of correlated  $\zeta^{\text{ib}}$  fluctuations are relatively more localized or regionalized, show smoother, more gradual boundaries, and are multiply connected, with apparent far-field teleconnections. This underscores the role of ocean dynamics and nonlocal

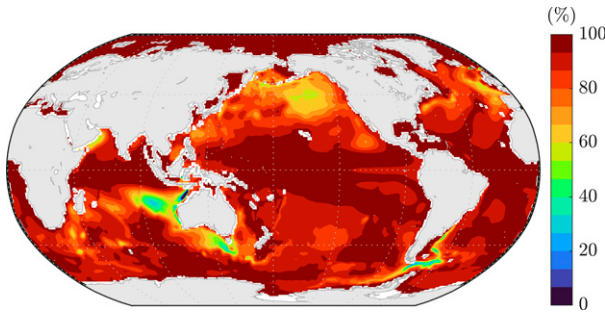


FIG. 8. Color shading indicates the percentage variance  $\mathcal{V}$  in monthly  $\zeta'$  explained by  $\zeta_m$ .

effects in establishing the dominant  $\zeta_m$  spatial covariance structure.

c. Vertical scales

Our interpretation mainly in terms of barotropic dynamics is corroborated by comparing modeled  $\zeta_m$  to simulated ocean dynamic sea level  $\zeta'$ . Changes in  $\zeta'$  identify changes in sea surface height above the geoid with the IB correction made (Gregory et al. 2019). For a purely barotropic response, subsurface pressure signals are vertically uniform (Gill 1982), and  $\zeta'$  and  $\zeta_m$  variations are equal (Vinogradova et al. 2007). Differences between  $\zeta'$  and  $\zeta_m$  changes, which represent changes in steric sea level  $\zeta_p$  arising from density changes at constant mass (Gregory et al. 2019), indicate baroclinic contributions to the ocean's adjustment. Since our model simulations represent the full primitive equations, including density and stratification effects, the  $\zeta'$  response to  $p_a$  can, in principle, involve both  $\zeta_m$  and  $\zeta_p$  processes.

Over much of the ocean,  $\zeta_m$  explains a majority of local monthly  $\zeta'$  variability (Fig. 8), indicating a largely barotropic response. More quantitatively,  $\zeta_m$  accounts for  $>80\%$  of the  $\zeta'$  variance in 88% of grid cells, where we define the percent variance  $\mathcal{V}$  in  $x$  explained by  $y$  as

$$\mathcal{V} \doteq 100\% \times \left( 1 - \frac{\sigma_{x-y}^2}{\sigma_x^2} \right), \quad (5)$$

where  $\sigma^2$  is variance. These results are qualitatively consistent with basic expectations from analytical theory for a stratified ocean forced by  $p_a$  (Ponte 1992; Wunsch and Stammer 1997). However, in some regions,  $\zeta_m$  fails to account for most of the  $\zeta'$  variance. Across parts of the extratropical Pacific Basin, Arabian Sea, southern tropical Indian Ocean, Wharton Basin abutting the Indonesian Throughflow, extratropical North Atlantic and Iberian Basins, slope regions of the Argentine Basin and Scotia Sea adjacent to the Patagonia Shelf, and parts of the South Australian Basin and Tasman Sea around Tasmania,  $\zeta_m$  explains  $\leq 60\%$  of the local  $\zeta'$  variance (Fig. 8). In these regions,  $\sigma_{\zeta_p}$  values can be  $\geq 60\%$  as large as  $\sigma_{\zeta'}$  values (Fig. 9).

The relative contributions of  $\zeta_p$  to  $\zeta'$  variability here are larger than reported in past studies. In their global modeling investigation of stratification effects on the large-scale ocean

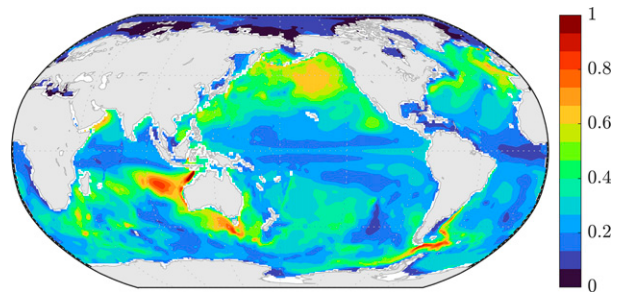


FIG. 9. Color shading indicates ratios of  $\sigma_{\zeta_p}$  to  $\sigma_{\zeta'}$ .

response to  $p_a$ , Ponte and Vinogradov (2007) find  $\sigma_{\zeta_p}/\sigma_{\zeta'}$  values up to  $\sim 0.1$ – $0.2$  but more typically  $\sim 0.01$ – $0.02$ . This contrasts with  $\sigma_{\zeta_p}/\sigma_{\zeta'}$  values in Fig. 9, which have a spatial mean of  $\sim 0.3$  and can reach  $>1$  in the most extreme cases. Importantly, whereas we analyze monthly model output generated from a 25-yr numerical integration, Ponte and Vinogradov (2007) study 6-hourly values from a 1-yr simulation. Since baroclinic effects generally become more important at longer periods (Vinogradova et al. 2007), such contrasts are therefore not entirely surprising. Even so, the details of the patterns of  $\zeta_p$  contributions to  $\zeta'$  variability are nontrivial and warrant further investigation. A thorough inquiry into  $\zeta_p$  is beyond our scope, given our primary focus on  $\zeta_m$  and the small amplitudes of these  $\zeta_p$  signals. However, we speculate that topographic interactions may be involved where  $\zeta_p$  effects are important and bathymetry is abrupt (e.g., Indonesian Throughflow), and vertical heaving may be implicated where background stratification is strong (e.g., southern tropical Indian Ocean). Small differences in surface heat and freshwater fluxes between the two simulations, touched on earlier, may also be involved.

d. Time scales

Spectral analysis sheds more light on  $\zeta_m$  variability and its relation to  $\zeta^{ib}$  and  $\zeta'$  fluctuations. Figure 10 shows power spectral densities of  $\zeta^{ib}$ ,  $\zeta_m$ ,  $\zeta'$ , and  $\zeta_p$  spatially averaged over the ocean. Aside from clear annual and semiannual signals, and possibly a harmonic partial at the 4-month period, the global-mean power spectral density of  $\zeta^{ib}$  looks essentially white, with roughly equal power across all nonseasonal frequencies. This corroborates basic expectations for white-noise atmospheric spectra at periods longer than a couple weeks (Frankignoul and Hasselmann 1977; Frankignoul and Müller 1979; Willebrand 1978). In contrast, while it also exhibits seasonal peaks,<sup>4</sup> the globally averaged spectrum of  $\zeta_m$  features decreasing power with decreasing frequency. Global-mean power in  $\zeta_m$  is  $\sim 1\%$  as large as  $\zeta^{ib}$  power at time scales  $\sim 2$  months and  $\leq 0.1\%$  as large at time scales  $\geq 2$  years (Fig. 10). Generally, such spectral behavior is predicted from the  $\omega$  dependence in (4) and agrees with intuition that deviations from an isostatic

<sup>4</sup> Averaging over the ocean, we find that the seasonal cycle typically explains  $\sim 10\%$  of the total variance in monthly  $\zeta_m$  at the model grid cell.

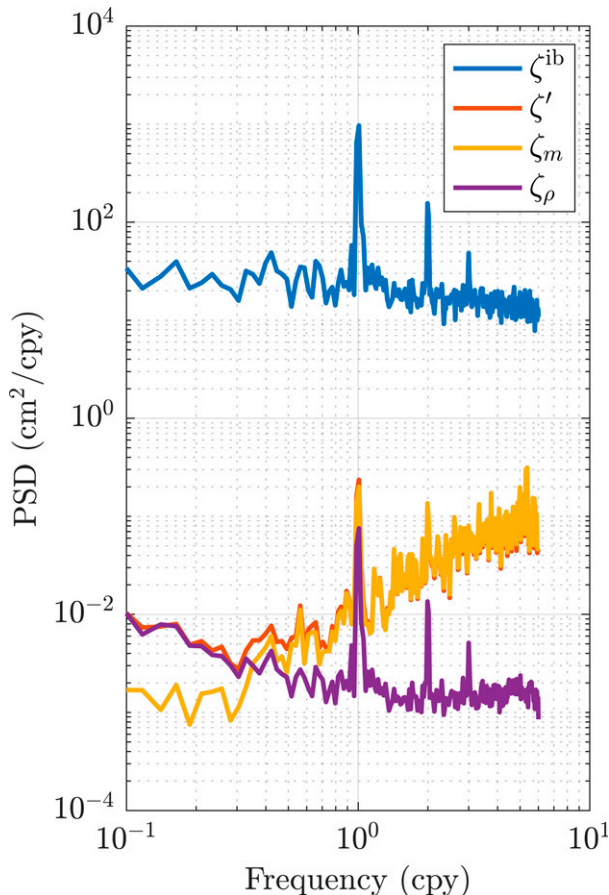


FIG. 10. Global-mean power spectral densities for  $\zeta^{\text{ib}}$  (blue),  $\zeta'$  (red),  $\zeta_m$  (yellow), and  $\zeta_\rho$  (purple). The cpy acronym stands for cycles per year.

response to  $p_a$ , quantified in terms of  $\zeta_m$ , become smaller at longer periods (Ponte et al. 1991).

For periods from a couple months to a few years, global-mean spectra of  $\zeta_m$  and  $\zeta'$  are basically identical (Fig. 10). Since  $\zeta_m$  and  $\zeta'$  variance is concentrated at short periods, this reemphasizes that monthly  $\zeta'$  variance is largely barotropic and explained by  $\zeta_m$  (Fig. 8). However, the tight coupling between global-mean  $\zeta_m$  and  $\zeta'$  spectra breaks down for periods longer than a few years. At the longest periods  $\sim 1$  decade,  $\zeta'$  power increases with decreasing frequency, such that power spectral densities for  $\zeta'$  and  $\zeta_\rho$  are comparable to one another, and larger than for  $\zeta_m$  (Fig. 10). The “crossover time scale” is when  $\zeta_m$  and  $\zeta_\rho$  effects on  $p_a$ -driven  $\zeta'$  are about equal is  $\sim 5$ –7 years. This is somewhat different from past studies reasoning that the ocean’s response to atmospheric forcing becomes essentially baroclinic by shorter time scales  $\sim 1$  year (Willebrand et al. 1980; Quinn and Ponte 2012; Vinogradova et al. 2007). The reason for this difference may be that  $p_a$  has larger scales and projects more strongly onto the barotropic mode than do other forcing functions like wind stress and buoyancy flux that tend to be the focus in studies on the vertical structure of ocean variability.

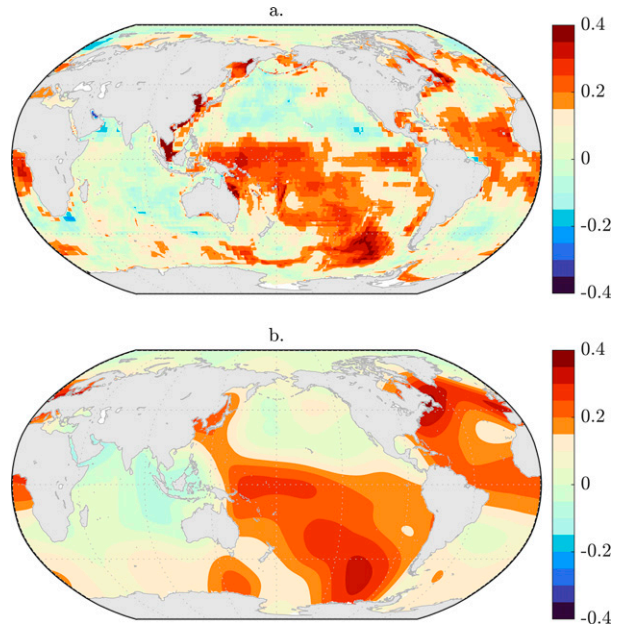


FIG. 11. (a) Color shading indicates correlation coefficients between  $\zeta_m^E$  from the model simulations and  $\zeta_m^G$  from GRACE mass data. Lightly shaded values have magnitudes  $\leq 0.15$  and are not distinguishable from zero at the 95% confidence level. (b) As in (a), but with a  $10^\circ$  isotropic Gaussian smoothing kernel applied to ECCO and GRACE before calculating correlation coefficients.

#### e. Relation to observations

Having established the dominant magnitudes and scales of low-frequency  $\zeta_m$  variability due to  $p_a$  loading, it remains to determine whether such behavior is relevant for interpretation of satellite gravimetry data over the ocean. To quantify the correspondence between modeled and observed signals in terms of phase and amplitude, we compute Pearson correlation coefficients and ratios of modeled to observed  $\sigma_{\zeta_m}$  between ECCO simulations and GRACE observations (Figs. 11 and 12). To avoid confusion, we use  $E$  and  $G$  superscripts to identify  $\zeta_m$  from model and data, respectively. Whereas  $\zeta_m^E$  fluctuations arise solely from  $p_a$  forcing,  $\zeta_m^G$  variations result from  $p_a$  forcing as well as other dynamic and isostatic effects, such as the ocean response to wind and freshwater flux, and changes in Earth’s gravitation, rotation, and deformation. If correlation coefficients and  $\sigma_{\zeta_m^E}/\sigma_{\zeta_m^G}$  values are both  $\sim 1$ , it means that  $p_a$  forcing makes primary contributions to behavior observed by GRACE, while  $\sigma_{\zeta_m^E}/\sigma_{\zeta_m^G}$  and correlations both  $\sim 0$  imply that  $p_a$  contributions to GRACE signals are negligible compared to other driving mechanisms.

Significant correlations are observed between  $\zeta_m^E$  and  $\zeta_m^G$  across broad swaths of the ocean (Fig. 11a). For reference, values with magnitudes  $\geq 0.15$  are distinguishable from zero at the 95% confidence level. Elevated values 0.2–0.3 are apparent in open-ocean regions, including over the Amundsen–Bellingshausen Basin in the Pacific sector of the Southern Ocean, and across much of the tropical Pacific and Atlantic Oceans. Strong correlations 0.2–0.4 are also found in marginal



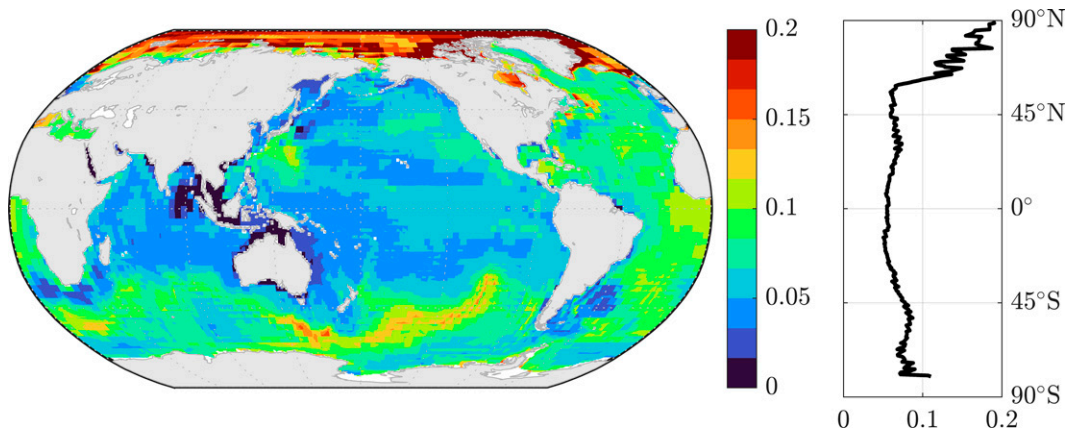


FIG. 12. Color shading indicates ratios of  $\sigma_m^E$  to  $\sigma_m^G$ . The right panel shows zonally averaged values.

seas in the western Pacific Ocean such as the Gulf of Thailand, Yellow Sea, and Sea of Okhotsk. Shelf and slope regions in the North Atlantic Ocean also feature enhanced coefficients 0.2–0.3, namely, small areas over the Greenland–Scotland Ridge, within the Labrador Sea and Baffin Bay, and over the Grand Banks off Newfoundland and Labrador in Canada. Significant negative correlations appear in the Arabian Sea and Persian Gulf, off South Africa, and over the Nordic Seas—such behavior may reflect random chance given the confidence levels used to assess significance, and it remains to be determined whether these instances identify true antiphase relationships between  $\zeta_m^E$  and  $\zeta_m^G$ . If fields are spatially smoothed, correlation coefficients between  $\zeta_m^E$  and  $\zeta_m^G$  increase (Fig. 11b), consistent with theoretical expectations [cf. Fig. 13 and Eq. (6) below].

Ratios of  $\sigma_m^E$  to  $\sigma_m^G$  range between  $<0.01$  and  $>0.20$  depending on location (Fig. 12). Typical  $\sigma_m^E/\sigma_m^G$  values over the

ocean are 0.05–0.08. Basin-scale structure is apparent, such that ratios over the Atlantic and Southern Oceans 0.07–0.08 are generally larger than those over the Pacific and Indian Oceans 0.04–0.05. The largest values  $\sigma_m^E/\sigma_m^G \geq 0.15$  are observed over the Arctic Ocean, Nordic Seas, and Hudson Bay. Especially noteworthy are ratios  $\geq 0.20$  around the Canadian Archipelago and Greenland, namely, in the Beaufort Sea, Canadian Basin, Lincoln Sea, Fram Strait, and Greenland Sea. Other areas with elevated values  $\sim 0.10$  include the slope of the Grand Banks and midocean ridges in the Southern Ocean. In contrast, smaller values  $\sigma_m^E/\sigma_m^G \leq 0.03$  are seen over the Zapiola Rise in the Argentine Basin, across the Gulf of Carpentaria and the Arafura Sea north of Australia, along the Izu Arc off Japan, within the Gulf of Thailand and around Indonesia, as well as inside the Red Sea and Persian Gulf. These ratios may signify strong ocean variation due to other forcing mechanisms, or nonocean signals in GRACE mass data over the ocean (e.g., Tōhoku and Sumatra–Andaman earthquakes, leakage of terrestrial water storage).

Most past studies interpret intraseasonal-to-interannual  $\zeta_m^G$  variations in terms of wind stress  $\tau$  forcing (see discussion for more details). Assuming that  $\tau$  is the most important driver of  $\zeta_m^G$  on these time scales, and assuming that  $\tau$ -driven and  $p_a$ -forced  $\zeta_m$  signals have comparable spatial scales, we develop a simple theory for the ratio of local  $p_a$  to  $\tau$  forcing to interpret the  $\sigma_m^E/\sigma_m^G$  values in Fig. 12. It follows from mass and momentum conservation in a linear, frictionless, barotropic ocean that the gain of the transfer function between  $\zeta_m$  signals forced by  $p_a$  and  $\tau$  is (see appendix C for a derivation)

$$\mathcal{G}(p_a, \tau) = \frac{\omega f^3 \rho_a}{2^{3/2} g C_D L^3 \bar{p}_a}, \quad (6)$$

where  $\rho_a$  is air density,  $C_D$  is a drag coefficient, and  $L$  and  $\bar{p}_a$  are a dominant wavenumber and representative magnitude of  $p_a$  variation, respectively. As defined in (6), for fixed  $\bar{p}_a$ ,  $\mathcal{G}$  increases (meaning that  $p_a$  becomes relatively more important compared to  $\tau$ ) with latitude, scale, and frequency. Consistent with (6),  $\sigma_m^E/\sigma_m^G$  values show latitudinal dependence, increasing from an average value of  $\sim 0.05$  between  $0^\circ$  and  $20^\circ$

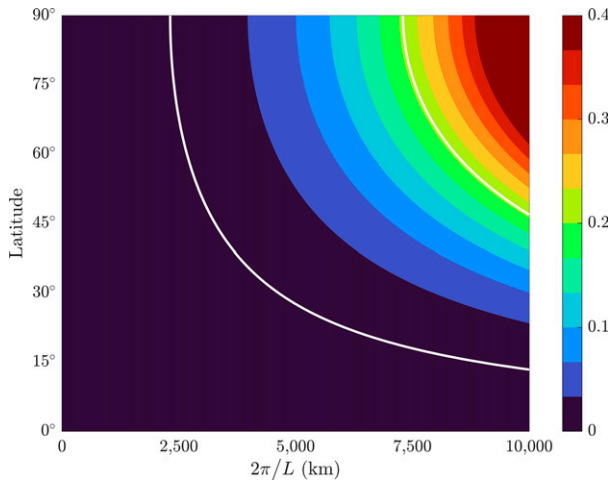


FIG. 13. Values of the gain of the transfer function  $\mathcal{G} = \omega f^3 \rho_a / (2^{3/2} g C_D L^3 \bar{p}_a)$  for variable  $L$  and latitude (6). Values are averaged over frequencies between  $\omega = 0$  and  $\omega = 2\pi/2$  months (the Nyquist angular frequency of GRACE). White contours identify values of 0.01 and 0.19, which are the 0.5th and 99.5th percentiles of values in Fig. 12.

latitude to  $\sim 0.07$  between  $30^\circ$  and  $50^\circ$  and  $\sim 0.09$  between  $60^\circ$  and  $80^\circ$  (Fig. 12). More quantitatively, 99% of  $\sigma_{\zeta_m^e}/\sigma_{\zeta_m^c}$  values shown in Fig. 12 fall between 0.01 and 0.19. A similar range of values is anticipated from (4) at monthly and longer time scales outside of the tropics for spatial scales  $2\pi/L$  2000–10 000 km assuming a representative amplitude of  $\bar{p}_a \sim 5$  hPa (Fig. 13). Note that  $p_a$  fluctuations show similar spatial correlation scales on the order of a few thousand kilometers (Fig. 7).

These results suggest that theory embodied by (6) provides a lowest-order description of the relative role of  $p_a$  loading in generating mass signals over the ocean observed by GRACE. While they are less important than  $\tau$  contributions,  $p_a$  contributions to monthly  $\zeta_m$  fluctuations are on the same order of magnitude as contributions from surface freshwater fluxes (Dobslaw and Thomas 2007; Peralta-Ferriz and Morison 2010; Piecuch and Wadehra 2020) and changes in Earth gravitation, rotation, and deformation (Adhikari et al. 2019). Thus, loading by  $p_a$  constitutes a secondary but nevertheless important contributor to monthly  $\zeta_m$  variability, which should be accounted for in comprehensive, quantitative attributions of mass changes observed by GRACE satellite gravimetry over the ocean.

#### 4. Discussion

We used twin global ocean model experiments, performed in the context of the Estimating the Circulation and Climate of the Ocean (ECCO) project, to quantify the dominant magnitudes and scales of the low-frequency dynamic manometric sea level  $\zeta_m$  response to barometric-pressure  $p_a$  loading (Figs. 3–10). We also determined the correspondence between modeled  $\zeta_m$  fluctuations driven by variable  $p_a$  and variations in  $\zeta_m$  from the Gravity Recovery and Climate Experiment (GRACE) arising from changes  $p_a$  and other dynamic and isostatic processes (Figs. 11, 12). Findings were interpreted in light of simple scaling arguments from barotropic potential vorticity conservation (Figs. 1, 13). Our results complement past studies, identify open questions, and point to possible avenues of future work.

Past studies of the large-scale, intraseasonal-to-interannual ocean response based on satellite gravimetry find elevated  $\zeta_m$  signals in the same continental-shelf, marginal-sea, and abyssal-plain regions highlighted here, largely ascribing them to wind forcing (Bingham and Hughes 2006; Boening et al. 2011; Bonin and Chambers 2011; Chambers 2011; Fukumori et al. 2015; Landerer and Volkov 2013; Quinn and Ponte 2011, 2012; Peralta-Ferriz et al. 2014; Piecuch et al. 2013; Piecuch and Ponte 2015; Ponte et al. 2007; Ponte and Piecuch 2014; Volkov 2014; Volkov and Landerer 2013). Likewise, past  $\zeta$  studies using altimetry and models also point to the Amundsen–Bellingshausen, Australian–Antarctic, Weddell–Enderby, and Pacific Basins as hotspots of barotropic variability on periods ranging from hours to months, with most interpreting these regional features in terms of highly damped geostrophic modes or topographically trapped Rossby waves forced by wind stress (Chao and Fu 1995; Fu 2003; Fu and Smith 1996; Fukumori et al. 1998; Stammer et al. 2000; Vivier et al. 2005;

Webb and de Cuevas 2002a,b, 2003; Weijer 2010; Weijer et al. 2009). By quantifying the secondary influence of  $p_a$  loading, we complement the literature stressing the primary role of wind forcing on the continental shelf, in marginal seas, and over abyssal plains.

Modeling studies on the ocean's dynamic response to variable  $p_a$  loading similarly identify strong  $\zeta_m$  variation on the continental shelf, in marginal seas, and over midlatitude abyssal plains (Greatbatch et al. 1996; Hirose et al. 2001; Mathers and Woodworth 2001; Ponte 1993, 1994, 1997, 2009; Ponte et al. 1991; Ponte and Vinogradov 2007; Stepanov and Hughes 2004, 2006; Tierney et al. 2000; Wright et al. 1987). These studies typically consider high-frequency output from short model integrations (e.g., 6-hourly values from a 1-yr simulation), which tend to emphasize shorter-period behavior. Models used in many of these studies also omit the Arctic Ocean. By interrogating lower-frequency output from a multidecadal global ocean model run, we thus add value to the literature by showing that subtle  $\zeta_m$  signals driven by  $p_a$  persist at monthly and longer periods, with strongest variability in and around the Arctic Ocean.

The findings of our spectral analysis are consistent with, but build upon, past modeling results. Earlier spectral analyses by Hirose et al. (2001), Ponte (1993), and Ponte and Vinogradov (2007), based on short integrations of global ocean models forced by  $p_a$  loading, establish that  $\zeta_m$  and  $\zeta'$  power increases with decreasing frequency for periods from  $\sim 1$  day to  $\sim 1$  week, and thereafter decreases with decreasing frequency for periods from a couple weeks to a few months. They also clarify that  $\zeta_p$  effects on  $\zeta'$  variations are small on these time scales. By showing that  $\zeta_m$  and  $\zeta'$  have decreasing power with decreasing frequency and are tightly coupled to each other on periods from a couple months to a few years, and demonstrating that  $\zeta_p$  changes and baroclinic effects contribute more importantly to  $\zeta'$  variations at longer time scales approaching  $\sim 1$  decade, we thus corroborate and extend previous findings.

The dynamic ocean response to variable  $p_a$  loading in the Arctic Ocean over monthly and longer periods has not received much attention in the literature. Past studies on the dynamic ocean response to  $p_a$  may have overlooked these signals because models used in those studies often omit the Arctic Ocean. An exception is Stepanov and Hughes (2006), whose barotropic model includes the Arctic Ocean. However, their discussion focuses on exchange between the Atlantic, Pacific, and Southern Oceans, and only peripherally addresses behavior in the Arctic Ocean. The Stepanov and Hughes (2006) model also includes wind forcing, so the role of  $p_a$  cannot be inferred unambiguously from their results. Past GRACE studies also largely omit discussion of  $p_a$  forcing in this region. The only exception we are aware of is Peralta-Ferriz and Morison (2010), who include  $p_a$  in their analytical model of the annual cycle in  $p_b$  averaged over the Arctic Ocean from GRACE during 2002–08. However, the annual cycle only accounts for 15% of the monthly data variance in their study, so it remains to be determined whether the frictional processes described by those authors apply to other time scales more generally. Furthermore, since their model is formulated in terms of a basin average, it does not shed light onto the

spatial structure of the oceanic response within the Arctic Ocean. Thus, future studies should interrogate  $p_a$ -driven  $\zeta_m$  variability in the Arctic Ocean in more detail, identifying the relevant forcing regions and elucidating the details of the dynamic response.

Our interpretation of the low-frequency dynamic ocean response to  $p_a$  was largely in terms of barotropic processes. This interpretation was supported by comparison between  $\zeta_m$  and ocean dynamic sea level  $\zeta'$  from the ECCO experiments (Fig. 8). However, we found that baroclinic effects and changes in steric sea level  $\zeta_\rho$  can be important for understanding the  $\zeta'$  response to  $p_a$  in some regions and on longer time scales, generally (Fig. 9). Since our primary focus was on  $\zeta_m$  behavior and satellite gravity data on monthly to decadal time scales, we deferred a thorough investigation of the mechanisms of  $\zeta_\rho$  variability due to variable  $p_a$  loading. This topic could be taken up in future studies.

Contrary to popular belief that floating ice has no effect on sea level, past studies establish that sea ice drives a thermodynamic ocean response and  $\zeta_\rho$  changes. Specifically, melting ice freshens the ocean, leading to  $\zeta_\rho$  increase related to the salinity decrease (Fukumori et al. 2021; Jenkins and Holland 2007; Munk 2003; Noerdlinger and Brower 2007; Shepherd et al. 2010). What has not, to our knowledge, been recognized is that changes in sea ice may also excite a dynamic ocean adjustment and  $\zeta_m$  changes. Changes in sea ice loading due to melting and freezing from freshwater fluxes with the ocean have no dynamical effect—since changes in the sea ice load are exactly balanced by the variable load implied by the surface freshwater flux itself, the ocean responds isostatically (Campin et al. 2008; Gill 1982; Gregory et al. 2019; Griffies and Greatbatch 2012). In contrast, any changes in sea ice loading related to sublimation and snowfall or lateral convergence or divergence of sea ice and snow that are not balanced by compensating  $p_a$  changes would imply a net load on the ocean that forces a dynamic ocean response analogous to the effects of  $p_a$  studied here. A follow-on study should be undertaken using model experiments to establish magnitudes and spatiotemporal scales of the dynamic ocean response to net loading by sea ice changes and ice–ocean freshwater fluxes in combination with  $p_a$  loading, and if such effects are relevant to interpretation of GRACE data over the Arctic and Southern Oceans.

*Acknowledgments.* The authors acknowledge support from the National Aeronautics and Space Administration through the GRACE Follow-On Science Team (Grant 80NSSC20K0728) and the Sea Level Change Team (Grant 80NSSC20K1241). The contribution from I. F. and O. W. represents research carried out at the Jet Propulsion Laboratory, California Institute of Technology, under a contract with the National Aeronautics and Space Administration (Grant 80NM0018D0004).

*Data availability statement.* Observational data and model output studied here are available through <https://ecco-group.org/products.htm> and <https://grace.jpl.nasa.gov/>. MATLAB codes used to produce the results are available from C. G. P. upon request.

## APPENDIX A

### Dynamic Manometric Sea Level $\zeta_m$

The definition of  $\zeta_m$  in Eq. (2) is equivalent to the “dynamic bottom pressure” from Stepanov and Hughes (2006) and identical to the “dynamic bottom pressure ... in terms of the equivalent sea level” from Ponte and Vinogradov (2007). While “dynamic” appears in its name,  $\zeta_m$  is not a purely dynamical quantity. For example, a horizontally uniform global-mean  $\zeta_m$  rise resulting from melting glaciers and ice sheets does not participate in ocean dynamics. The definition of  $\zeta_m$  in Eq. (2) is similar to the definition of manometric sea level from Gregory et al. (2019) [see their note (N18) and Eqs. (33) and (36)]. The difference between the definitions is that manometric sea level includes the IB effect (Fig. 3 in Gregory et al. 2019) whereas  $\zeta_m$  does not. In other words, manometric sea level measures the mass of the oceanic water column whereas  $\zeta_m$  measures the mass of the combined oceanic–atmospheric fluid column above the seafloor. We consider  $\zeta_m$  rather than manometric sea level given our focus on ocean dynamics.

## APPENDIX B

### Derivation of Potential Vorticity Equation and Transfer Function

Starting from the depth-integrated linear momentum and mass continuity equations

$$\frac{\partial \mathbf{U}}{\partial t} + f \hat{\mathbf{z}} \times \mathbf{U} = \mathbf{F}, \tag{B1}$$

$$\nabla \cdot \mathbf{U} = Q - \frac{\partial M}{\partial t}, \tag{B2}$$

Hughes (2008) derives the following form of potential vorticity equation for depth-integrated flow

$$\begin{aligned} \frac{1}{g} \frac{\partial p_b}{\partial t} - \nabla \cdot \left( \frac{H}{f^2} \nabla \frac{\partial p_b}{\partial t} \right) + \mathbf{J} \left( p_b, \frac{H}{f} \right) &= Q + \frac{1}{g} \frac{\partial p_a}{\partial t} \\ - \nabla \times \left( \frac{\boldsymbol{\tau}}{f} \right) - \mathbf{J} \left( E, \frac{1}{f} \right) + \nabla \cdot \left[ \frac{1}{f^2} \frac{\partial}{\partial t} (\nabla E - \boldsymbol{\tau}) \right]. \end{aligned} \tag{B3}$$

Here  $\mathbf{U} \doteq \int_{-H}^{\zeta} \rho \mathbf{u} dz$  is depth-integrated mass transport with horizontal velocity  $\mathbf{u}$  and density  $\rho$ ,  $\mathbf{F} \doteq \boldsymbol{\tau} - \int_{-H}^{\zeta} \nabla p dz$  is horizontal force per unit area with wind stress  $\boldsymbol{\tau}$ ,  $Q$  is mass source per unit area,  $M \doteq (p_b - p_a)/g$  is ocean mass per unit area,  $E \doteq \int_{-H}^0 \rho g z dz$  is potential energy per unit area, and  $\hat{\mathbf{z}}$  is the vertical unit vector. All other symbols are defined above. As explained by Hughes (2008), (B3) is, “the most general form of a linear barotropic potential vorticity equation in a single scalar variable,” applicable to subinertial motions. Interested readers are referred to Hughes (2008) for details on the derivation of (B3) from (B1) and (B2).

We derive a reduced form of (B3) for studying the large-scale, low-frequency  $\zeta_m$  response to  $p_a$  in the context of satellite gravimetry. Ignoring mass sources, wind stress, and

stratification, we obtain a potential vorticity equation for a barotropic ocean forced by  $p_a$  loading

$$\frac{1}{g} \frac{\partial p_b}{\partial t} - \nabla \cdot \left( \frac{H}{f^2} \nabla \frac{\partial p_b}{\partial t} \right) + \mathbf{J} \left( p_b, \frac{H}{f} \right) = \frac{1}{g} \frac{\partial p_a}{\partial t}. \quad (\text{B4})$$

Dividing by  $\rho_0$  and subtracting  $\bar{p}_a$  from both sides, we express (B4) in terms of  $\zeta_m$  and  $\zeta^{\text{ib}}$

$$\frac{\partial \zeta_m}{\partial t} - g \nabla \cdot \left( \frac{H}{f^2} \nabla \frac{\partial \zeta_m}{\partial t} \right) + g \mathbf{J} \left( \zeta_m, \frac{H}{f} \right) = -\frac{\partial \zeta^{\text{ib}}}{\partial t}, \quad (\text{B5})$$

by virtue of (1) and (2). Note that, to write relative-vorticity generation (second term on the left) and the Jacobian determinant (third term on the left) in terms of  $\zeta_m$ , we subtract  $\bar{p}_a$  and  $\bar{p}_a$  from under their respective spatial derivatives, which is allowed as both are horizontally uniform.

We perform a dimensional analysis to simplify (B5) for the space and time scales under study. The ratio of relative-vorticity generation to the Jacobian determinant goes like  $\omega/f$ , whereas the ratio of stretching (first term on the left of B5) to the Jacobian determinant goes like  $\omega \ell^2 / f \ell_R^2$ , where  $\ell$  is a length scale and  $\ell_R \doteq \sqrt{gH}/f$  is the barotropic Rossby radius of deformation. Considering the monthly periods and basin scales observed by GRACE, and assuming a typical midlatitude value of  $f \approx 1 \times 10^{-4} \text{ s}^{-1}$  and representative ocean depth  $H \approx 4000 \text{ m}$ , we obtain that  $\omega/f \ll 1$  and  $\omega \ell^2 / f \ell_R^2 \ll 1$ , meaning that stretching and relative-vorticity generation are small compared to the Jacobian determinant. Ignoring the former terms in (B5) gives the lowest-order potential vorticity equation in (3)

$$g \mathbf{J} \left( \zeta_m, \frac{H}{f} \right) = -\frac{\partial \zeta^{\text{ib}}}{\partial t}. \quad (\text{B6})$$

To obtain the transfer function in (4), we assume that  $\zeta_m$  and  $\zeta^{\text{ib}}$  are given by Fourier components (plane waves) of the form  $\exp[i(kx + ly - \omega t)]$  where  $\mathbf{k} \doteq k\hat{\mathbf{x}} + l\hat{\mathbf{y}}$  is horizontal wavenumber with zonal and meridional unit vectors  $\hat{\mathbf{x}}$  and  $\hat{\mathbf{y}}$ , respectively, and  $i \doteq \sqrt{-1}$ . Inserting wave forms into (3) and dividing by  $\zeta^{\text{ib}}$  yields

$$h(\zeta_m, \zeta^{\text{ib}}) = \frac{\mathcal{F}(\zeta_m)}{\mathcal{F}(\zeta^{\text{ib}})} = \frac{\omega}{g\mathbf{k} \times \nabla(H/f)}. \quad (\text{B7})$$

Defining  $\gamma \doteq |\nabla(H/f)|$  the magnitude of the  $H/f$  gradient and  $K$  the projection of  $\mathbf{k}$  along  $H/f$  contours [i.e., perpendicular to  $\nabla(H/f)$ ], we rewrite (B7) in the form of (4) from the main text

$$h(\zeta_m, \zeta^{\text{ib}}) = \frac{\mathcal{F}(\zeta_m)}{\mathcal{F}(\zeta^{\text{ib}})} = \frac{\omega}{gK\gamma}. \quad (\text{B8})$$

## APPENDIX C

### Transfer Function between $\zeta_m$ due to $p_a$ to $\tau$ Forcing

To understand the relationship between  $\zeta_m$  signals from the model and GRACE (Fig. 12), we formulate a theory

for the transfer function between  $p_a$ -driven and  $\tau$ -forced  $\zeta_m$  variation. According to (B3), the transfer function of  $p_a$  to  $\tau$  forcing of  $\zeta_m$  is

$$h(p_a, \tau) \doteq \frac{\mathcal{F}(p_a/g)}{\mathcal{F}(\nabla \times \tau/f)}. \quad (\text{C1})$$

Note that the denominator of (C1) omits a term related to the divergence of  $\tau$  tendency [cf. (B3)], which is small relative to  $\tau$  curl on monthly and longer time scales of interest here. To simplify (C1), we write  $\tau$  in terms of wind  $\mathbf{v}$

$$\tau = \rho_a C_D |\mathbf{v}| \mathbf{v}, \quad (\text{C2})$$

where  $\rho_a$  is air density,  $C_D$  is drag coefficient, and we ignore surface currents. We also assume that winds are geostrophic

$$\mathbf{v} = \frac{1}{f\rho_a} \hat{\mathbf{z}} \times \nabla p_a. \quad (\text{C3})$$

Inserting (C2) and (C3) into (C1), assuming  $p_a$  is given by plane waves, simplifying the resulting expression, and taking the magnitude yields the gain from (6) in the main text

$$\mathcal{G}(p_a, \tau) = \frac{\omega f^3 \rho_a}{2^{3/2} g C_D L^3 \bar{p}_a}, \quad (\text{C4})$$

where  $\bar{p}_a$  is a real constant representing the magnitude of  $p_a$  variation and we define the isotropic wavenumber  $k = l = L$ . According to (C4),  $p_a$  becomes important relative to  $\tau$  for higher latitude, shorter periods, and larger scales. Figure 13 shows  $\mathcal{G}(p_a, \tau)$  values averaged over all frequencies between  $\omega = 0$  and  $\omega = 2\pi/2$  months as a function of latitude and  $L$  assuming reasonable values  $\rho_a \sim 1 \text{ kg m}^{-3}$ ,  $C_D \sim 1 \times 10^{-3}$ ,  $g \sim 10 \text{ m s}^{-2}$ , and  $\bar{p}_a \sim 5$ .

## REFERENCES

- Adhikari, S., E. R. Ivins, T. Frederikse, F. W. Landerer, and L. Caron, 2019: Sea-level fingerprints emergent from GRACE mission data. *Earth Syst. Sci. Data*, **11**, 629–646, <https://doi.org/10.5194/essd-11-629-2019>.
- Bingham, R. J., and C. W. Hughes, 2006: Observing seasonal bottom pressure variability in the North Pacific with GRACE. *Geophys. Res. Lett.*, **33**, L08607, <https://doi.org/10.1029/2005GL025489>.
- Boening, C., T. Lee, and V. Zlotnicki, 2011: A record-high ocean bottom pressure in the South Pacific observed by GRACE. *Geophys. Res. Lett.*, **38**, L04602, <https://doi.org/10.1029/2010GL046013>.
- Bonin, J. A., and D. P. Chambers, 2011: Evaluation of high-frequency oceanographic signal in GRACE data: Implications for de-aliasing. *Geophys. Res. Lett.*, **38**, L17608, <https://doi.org/10.1029/2011GL048881>.
- Brown, W., W. Munk, F. Snodgrass, H. Mofjeld, and B. Zetler, 1975: MODE bottom experiment. *J. Phys. Oceanogr.*, **5**, 75–85, [https://doi.org/10.1175/1520-0485\(1975\)005<0075:MBE>2.0.CO;2](https://doi.org/10.1175/1520-0485(1975)005<0075:MBE>2.0.CO;2).
- Campin, J.-M., J. Marshall, and D. Ferreira, 2008: Sea ice-ocean coupling using a rescaled vertical coordinate  $z^*$ . *Ocean*

- Modell.*, **24**, 1–14, <https://doi.org/10.1016/j.ocemod.2008.05.005>.
- Carrère, L., and F. Lyard, 2003: Modeling the barotropic response of the global ocean to atmospheric wind and pressure forcing—comparisons with observations. *Geophys. Res. Lett.*, **30**, 1275, <https://doi.org/10.1029/2002GL016473>.
- , Y. Faugère, and M. Ablain, 2016: Major improvement of altimetry sea level estimations using pressure-derived corrections based on ERA-Interim atmospheric reanalysis. *Ocean Sci.*, **12**, 825–842, <https://doi.org/10.5194/os-12-825-2016>.
- Chambers, D. P., 2011: ENSO-correlated fluctuations in ocean bottom pressure and wind-stress curl in the North Pacific. *Ocean Sci.*, **7**, 685–692, <https://doi.org/10.5194/os-7-685-2011>.
- , and J. K. Willis, 2009: Low-frequency exchange of mass between ocean basins. *J. Geophys. Res.*, **114**, C11008, <https://doi.org/10.1029/2009JC005518>.
- Chao, Y., and L.-L. Fu, 1995: A comparison between the TOPEX/POSEIDON data and a global ocean general circulation model during 1992–1993. *J. Geophys. Res.*, **100**, 24965–24976, <https://doi.org/10.1029/95JC02260>.
- Close, C., 1918: The fluctuations of mean sea-level with special reference to those caused by variations in barometric pressure. *Geogr. J.*, **52**, 51–58, <https://doi.org/10.2307/1779861>.
- Dee, D. P., and Coauthors, 2011: The ERA-Interim reanalysis: Configuration and performance of the data assimilation system. *Quart. J. Roy. Meteor. Soc.*, **137**, 553–597, <https://doi.org/10.1002/qj.828>.
- Dobslaw, H., and M. Thomas, 2007: Impact of river run-off on global ocean mass redistribution. *Geophys. J. Int.*, **168**, 527–532, <https://doi.org/10.1111/j.1365-246X.2006.03247.x>.
- Doodson, A. T., 1924: Meteorological perturbations of sea-level and tides. *Geophys. Suppl. Mon. Not. Roy. Astron. Soc.*, **1**, 124–147, <https://doi.org/10.1111/j.1365-246X.1924.tb05363.x>.
- Ferry, N., and Coauthors, 2012: GLORYS2V1 global ocean reanalysis of the altimetric era 1992–2009 at mesoscale. *Mercator Ocean Quarterly Newsletter*, No. 44, Mercator Ocean Office, Toulouse, France, 29–39, <https://www.mercator-ocean.eu/en/ocean-science/scientific-publications/mercator-ocean-journal/newsletter-44-various-areas-of-benefit-using-the-mercator-ocean-products/>.
- Forget, G., J.-M. Campin, P. Heimbach, C. N. Hill, R. M. Ponte, and C. Wunsch, 2015: ECCO version 4: An integrated framework for non-linear inverse modeling and global ocean state estimation. *Geosci. Model Dev.*, **8**, 3071–3104, <https://doi.org/10.5194/gmd-8-3071-2015>.
- , —, —, —, and —, 2016: ECCO Version 4: Second release. MIT Libraries, 147 pp., <http://hdl.handle.net/1721.1/102062>.
- Frankignoul, C., and K. Hasselmann, 1977: Stochastic climate models. Part II Application to sea-surface temperature anomalies and thermocline variability. *Tellus*, **29**, 289–305, <https://doi.org/10.3402/tellusa.v29i4.11362>.
- , and P. Müller, 1979: Quasi-geostrophic response of an infinite  $\beta$ -plane ocean to stochastic forcing by the atmosphere. *J. Phys. Oceanogr.*, **9**, 104–127, [https://doi.org/10.1175/1520-0485\(1979\)009<0104:QGROAI>2.0.CO;2](https://doi.org/10.1175/1520-0485(1979)009<0104:QGROAI>2.0.CO;2).
- , —, and E. Zorita, 1997: A simple model of the decadal response of the ocean to stochastic wind forcing. *J. Phys. Oceanogr.*, **27**, 1533–1546, [https://doi.org/10.1175/1520-0485\(1997\)027<1533:ASMOTD>2.0.CO;2](https://doi.org/10.1175/1520-0485(1997)027<1533:ASMOTD>2.0.CO;2).
- Fu, L.-L., 2003: Wind-forced intraseasonal sea-level variability of the extratropical oceans. *J. Phys. Oceanogr.*, **33**, 436–449, [https://doi.org/10.1175/1520-0485\(2003\)033<0436:WFISLV>2.0.CO;2](https://doi.org/10.1175/1520-0485(2003)033<0436:WFISLV>2.0.CO;2).
- , and G. Pihos, 1994: Determining the response of sea level to atmospheric pressure forcing using TOPEX/POSEIDON data. *J. Geophys. Res.*, **99**, 24633–24642, <https://doi.org/10.1029/94JC01647>.
- , and R. D. Smith, 1996: Global ocean circulation from satellite altimetry and high-resolution computer simulation. *Bull. Amer. Meteor. Soc.*, **77**, 2625–2636, [https://doi.org/10.1175/1520-0477\(1996\)077<2625:GOCFSA>2.0.CO;2](https://doi.org/10.1175/1520-0477(1996)077<2625:GOCFSA>2.0.CO;2).
- Fukumori, I., R. Raghunath, and L.-L. Fu, 1998: Nature of global large-scale sea level variability in relation to atmospheric forcing: A modeling study. *J. Geophys. Res.*, **103**, 5493–5512, <https://doi.org/10.1029/97JC02907>.
- , O. Wang, W. Llovel, I. Fenty, and G. Forget, 2015: A near-uniform fluctuation of ocean bottom pressure and sea level across the deep ocean basins of the Arctic Ocean and the Nordic Seas. *Prog. Oceanogr.*, **134**, 152–172, <https://doi.org/10.1016/j.pocan.2015.01.013>.
- , —, I. Fenty, G. Forget, P. Heimbach, and R. M. Ponte, 2017: ECCO Version 4 Release 3. MIT, 10 pp., <http://hdl.handle.net/1721.1/110380>.
- , —, and —, 2021: Causal mechanisms of sea level and freshwater content change in the Beaufort Sea. *J. Phys. Oceanogr.*, **51**, 3217–3234, <https://doi.org/10.1175/JPO-D-21-0069.1>.
- Gaspar, P., and R. M. Ponte, 1997: Relation between sea level and barometric pressure determined from altimeter data and model simulations. *J. Geophys. Res.*, **102**, 961–971, <https://doi.org/10.1029/96JC02920>.
- , Y. Grégoris, and J.-M. Lefevre, 1990: A simple eddy kinetic energy model for simulations of the oceanic vertical mixing: Tests at Station Papa and long-term upper ocean study site. *J. Geophys. Res.*, **95**, 16179–16193, <https://doi.org/10.1029/JC095iC09p16179>.
- Gent, P. R., and J. C. McWilliams, 1990: Isopycnal mixing in ocean circulation models. *J. Phys. Oceanogr.*, **20**, 150–155, [https://doi.org/10.1175/1520-0485\(1990\)020<0150:IMIOCM>2.0.CO;2](https://doi.org/10.1175/1520-0485(1990)020<0150:IMIOCM>2.0.CO;2).
- Gill, A. E., 1982: *Atmosphere–Ocean Dynamics*. Academic Press, 662 pp.
- , and P. P. Niler, 1973: The theory of the seasonal variability in the ocean. *Deep-Sea Res. Oceanogr. Abstr.*, **20**, 141–177, [https://doi.org/10.1016/0011-7471\(73\)90049-1](https://doi.org/10.1016/0011-7471(73)90049-1).
- Greatbatch, R. J., Y. Lu, and B. de Young, 1996: Application of a barotropic model to North Atlantic synoptic sea level variability. *J. Mar. Res.*, **54**, 451–469, <https://doi.org/10.1357/0022240963213501>.
- Gregory, J. M., and Coauthors, 2019: Concepts and terminology for sea level: Mean, variability and change, both local and global. *Surv. Geophys.*, **40**, 1251–1289, <https://doi.org/10.1007/s10712-019-09525-z>.
- Griffies, S. M., and R. J. Greatbatch, 2012: Physical processes that impact the evolution of global mean sea level in ocean climate models. *Ocean Modell.*, **51**, 37–72, <https://doi.org/10.1016/j.ocemod.2012.04.003>.
- Heimbach, P., C. Hill, and R. Giering, 2005: An efficient exact adjoint of the parallel MIT General Circulation Model, generated via automatic differentiation. *Future Gener. Comput. Syst.*, **21**, 1356–1371, <https://doi.org/10.1016/j.future.2004.11.010>.
- , and Coauthors, 2019: Putting it all together: Adding value to the global ocean and climate observing systems with complete self-consistent ocean state and parameter estimates.

- Front. Mar. Sci.*, **6**, 55, <https://doi.org/10.3389/fmars.2019.00055>.
- Hirose, N., I. Fukumori, V. Zlotnicki, and R. M. Ponte, 2001: Modeling the high-frequency barotropic response of the ocean to atmospheric disturbances: Sensitivity to forcing, topography, and friction. *J. Geophys. Res.*, **106**, 30987–30995, <https://doi.org/10.1029/2000JC000763>.
- Hughes, C. W., 2008: A form of potential vorticity equation for depth-integrated flow with a free surface. *J. Phys. Oceanogr.*, **38**, 1131–1136, <https://doi.org/10.1175/2007JPO3809.1>.
- , I. Fukumori, S. M. Griffies, J. M. Huthnance, S. Minobe, P. Spence, K. R. Thompson, and A. Wise, 2019: Sea level and the role of coastal trapped waves in mediating the influence of the open ocean on the coast. *Surv. Geophys.*, **40**, 1467–1492, <https://doi.org/10.1007/s10712-019-09535-x>.
- Jenkins, A., and D. Holland, 2007: Melting of floating ice and sea level rise. *Geophys. Res. Lett.*, **34**, L16609, <https://doi.org/10.1029/2007GL030784>.
- Köhl, A., 2015: Evaluation of the GECCO2 ocean synthesis: Transports of volume, heat and freshwater in the Atlantic. *Quart. J. Roy. Meteor. Soc.*, **141**, 166–181, <https://doi.org/10.1002/qj.2347>.
- Landerer, F. W., and D. L. Volkov, 2013: The anatomy of recent large sea level fluctuations in the Mediterranean Sea. *Geophys. Res. Lett.*, **40**, 553–557, <https://doi.org/10.1002/grl.50140>.
- , and Coauthors, 2020: Extending the global mass change data record: GRACE follow-on instrument and science data performance. *Geophys. Res. Lett.*, **47**, e2020GL088306, <https://doi.org/10.1029/2020GL088306>.
- Magaard, L., 1977: On the generation of baroclinic Rossby waves in the ocean by meteorological forces. *J. Phys. Oceanogr.*, **7**, 359–364, [https://doi.org/10.1175/1520-0485\(1977\)007<0359:OTGOBR>2.0.CO;2](https://doi.org/10.1175/1520-0485(1977)007<0359:OTGOBR>2.0.CO;2).
- Marshall, J., A. Adcroft, C. Hill, L. Perelman, and C. Heisey, 1997: A finite-volume, incompressible Navier Stokes model for studies of the ocean on parallel computers. *J. Geophys. Res.*, **102**, 5753–5766, <https://doi.org/10.1029/96JC02775>.
- Mathers, E. L., and P. L. Woodworth, 2001: Departures from the local inverse barometer model observed in altimeter and tide gauge data and in a global barotropic numerical model. *J. Geophys. Res.*, **106**, 6957–6972, <https://doi.org/10.1029/2000JC000241>.
- Munk, W., 2003: Ocean freshening, sea level rising. *Science*, **300**, 2041–2043, <https://doi.org/10.1126/science.1085534>.
- Noerdlinger, P. D., and K. R. Brower, 2007: The melting of floating ice raises the ocean level. *Geophys. J. Int.*, **170**, 145–150, <https://doi.org/10.1111/j.1365-246X.2007.03472.x>.
- Peralta-Ferriz, C., and J. Morison, 2010: Understanding the annual cycle of the Arctic Ocean bottom pressure. *Geophys. Res. Lett.*, **37**, L10603, <https://doi.org/10.1029/2010GL042827>.
- , J. H. Morison, J. M. Wallace, J. A. Bonin, and J. Zhang, 2014: Arctic ocean circulation patterns revealed by GRACE. *J. Climate*, **27**, 1445–1468, <https://doi.org/10.1175/JCLI-D-13-00013.1>.
- Philander, S. G. H., 1978: Forced oceanic waves. *Rev. Geophys.*, **16**, 15–46, <https://doi.org/10.1029/RG016i001p00015>.
- Piecuch, C. G., and R. M. Ponte, 2015: A wind-driven nonseasonal barotropic fluctuation of the Canadian inland seas. *Ocean Sci.*, **11**, 175–185, <https://doi.org/10.5194/os-11-175-2015>.
- , and R. Wadehra, 2020: Dynamic sea level variability due to seasonal river discharge: A preliminary global ocean model study. *Geophys. Res. Lett.*, **47**, e2020GL086984, <https://doi.org/10.1029/2020GL086984>.
- , K. J. Quinn, and R. M. Ponte, 2013: Satellite-derived interannual ocean bottom pressure variability and its relation to sea level. *Geophys. Res. Lett.*, **40**, 3106–3110, <https://doi.org/10.1002/grl.50549>.
- Ponte, R. M., 1992: The sea level response of a stratified ocean to barometric pressure forcing. *J. Phys. Oceanogr.*, **22**, 109–113, [https://doi.org/10.1175/1520-0485\(1992\)022<0109:TSLROA>2.0.CO;2](https://doi.org/10.1175/1520-0485(1992)022<0109:TSLROA>2.0.CO;2).
- , 1993: Variability in a homogeneous global ocean forced by barometric pressure. *Dyn. Atmos. Oceans*, **18**, 209–234, [https://doi.org/10.1016/0377-0265\(93\)90010-5](https://doi.org/10.1016/0377-0265(93)90010-5).
- , 1994: Understanding the relation between wind- and pressure-driven sea level variability. *J. Geophys. Res.*, **99**, 8033–8039, <https://doi.org/10.1029/94JC00217>.
- , 1997: Nonequilibrium response of the global ocean to the 5-day Rossby-Haurwitz wave in atmospheric surface pressure. *J. Phys. Oceanogr.*, **27**, 2158–2168, [https://doi.org/10.1175/1520-0485\(0\)027<2158:NROTGO>2.0.CO;2](https://doi.org/10.1175/1520-0485(0)027<2158:NROTGO>2.0.CO;2).
- , 2006: Low-frequency sea level variability and the inverted barometer effect. *J. Atmos. Oceanic Technol.*, **23**, 619–629, <https://doi.org/10.1175/JTECH1864.1>.
- , 2009: Rate of work done by atmospheric pressure on the ocean general circulation and tides. *J. Phys. Oceanogr.*, **39**, 458–464, <https://doi.org/10.1175/2008JPO4034.1>.
- , and P. Gaspar, 1999: Regional analysis of the inverted barometer effect over the global ocean using TOPEX/POSEIDON data and model results. *J. Geophys. Res.*, **104**, 15 587–15 601, <https://doi.org/10.1029/1999JC900113>.
- , and S. V. Vinogradov, 2007: Effects of stratification on the large-scale ocean response to barometric pressure. *J. Phys. Oceanogr.*, **37**, 245–258, <https://doi.org/10.1175/JPO3010.1>.
- , and C. G. Piecuch, 2014: Interannual bottom pressure signals in the Australian–Antarctic and Bellingshausen basins. *J. Phys. Oceanogr.*, **44**, 1456–1465, <https://doi.org/10.1175/JPO-D-13-0223.1>.
- , D. A. Salstein, and R. D. Rosen, 1991: Sea level response to pressure forcing in a barotropic numerical model. *J. Phys. Oceanogr.*, **21**, 1043–1057, [https://doi.org/10.1175/1520-0485\(1991\)021<1043:SLRTPF>2.0.CO;2](https://doi.org/10.1175/1520-0485(1991)021<1043:SLRTPF>2.0.CO;2).
- , K. J. Quinn, C. Wunsch, and P. Heimbach, 2007: A comparison of model and GRACE estimates of the large-scale seasonal cycle in ocean bottom pressure. *Geophys. Res. Lett.*, **34**, L09603, <https://doi.org/10.1029/2007GL029599>.
- Proudman, J., 1929: The effects on the sea of changes in atmospheric pressure. *Geophys. Suppl. Mon. Not. Roy. Astron. Soc.*, **2**, 197–209, <https://doi.org/10.1111/j.1365-246X.1929.tb05408.x>.
- Quinn, K. J., and R. M. Ponte, 2011: Estimating high frequency ocean bottom pressure variability. *Geophys. Res. Lett.*, **38**, L08611, <https://doi.org/10.1029/2010GL046537>.
- , and —, 2012: High frequency barotropic ocean variability observed by GRACE and satellite altimetry. *Geophys. Res. Lett.*, **39**, L07603, <https://doi.org/10.1029/2012GL051301>.
- Redi, M. H., 1982: Oceanic isopycnal mixing by coordinate rotation. *J. Phys. Oceanogr.*, **12**, 1154–1158, [https://doi.org/10.1175/1520-0485\(1982\)012<1154:OIMBCR>2.0.CO;2](https://doi.org/10.1175/1520-0485(1982)012<1154:OIMBCR>2.0.CO;2).
- Shepherd, A., D. Wingham, D. Wallis, K. Giles, S. Laxon, and A. V. Sundal, 2010: Recent loss of floating ice and the consequent sea level contribution. *Geophys. Res. Lett.*, **37**, L13503, <https://doi.org/10.1029/2010GL042496>.
- Stammer, D., C. Wunsch, and R. M. Ponte, 2000: De-aliasing of global high frequency barotropic motions in altimeter

- observations. *Geophys. Res. Lett.*, **27**, 1175–1178, <https://doi.org/10.1029/1999GL011263>.
- Stepanov, V. N., and C. W. Hughes, 2004: Parameterization of ocean self-attraction and loading in numerical models of the ocean circulation. *J. Geophys. Res.*, **109**, C03037, <https://doi.org/10.1029/2003JC002034>.
- , and —, 2006: Propagation of signals in basin-scale ocean bottom pressure from a barotropic model. *J. Geophys. Res.*, **111**, C12002, <https://doi.org/10.1029/2005JC003450>.
- Storto, A., S. Masina, and A. Navarra, 2016: Evaluation of the CMCC eddy-permitting global ocean physical reanalysis system (C-GLORES, 1982–2012) and its assimilation components. *Quart. J. Roy. Meteor. Soc.*, **142**, 738–758, <https://doi.org/10.1002/qj.2673>.
- Tapley, B. D., and Coauthors, 2019: Contributions of GRACE to understanding climate change. *Nat. Climate Change*, **9**, 358–369, <https://doi.org/10.1038/s41558-019-0456-2>.
- Tierney, C., J. Wahr, F. Bryan, and V. Zlotnicki, 2000: Short-period oceanic circulation: Implications for satellite altimetry. *Geophys. Res. Lett.*, **27**, 1255–1258, <https://doi.org/10.1029/1999GL010507>.
- VanDam, T. M., and J. Wahr, 1993: The atmospheric load response of the ocean determined using Geosat altimeter data. *Geophys. J. Int.*, **113**, 1–16, <https://doi.org/10.1111/j.1365-246X.1993.tb02524.x>.
- Vinogradova, N. T., R. M. Ponte, and D. Stammer, 2007: Relation between sea level and bottom pressure and the vertical dependence of oceanic variability. *Geophys. Res. Lett.*, **34**, L03608, <https://doi.org/10.1029/2006GL028588>.
- Vivier, F., K. A. Kelly, and M. Harismendy, 2005: Causes of large-scale sea level variations in the Southern Ocean: Analyses of sea level and a barotropic model. *J. Geophys. Res.*, **110**, C09014, <https://doi.org/10.1029/2004JC002773>.
- Volkov, D. L., 2014: Do the North Atlantic winds drive the non-seasonal variability of the Arctic Ocean sea level? *Geophys. Res. Lett.*, **41**, 2041–2047, <https://doi.org/10.1002/2013GL059065>.
- , and F. W. Landerer, 2013: Nonseasonal fluctuations of the Arctic Ocean mass observed by the GRACE satellites. *J. Geophys. Res. Oceans*, **118**, 6451–6460, <https://doi.org/10.1002/2013JC009341>.
- Watkins, M. M., D. N. Wiese, D.-H. Yuan, C. Boening, and F. W. Landerer, 2015: Improved methods for observing Earth's time variable mass distribution with GRACE using spherical cap mascons. *J. Geophys. Res. Solid Earth*, **120**, 2648–2671, <https://doi.org/10.1002/2014JB011547>.
- Webb, D. J., and B. A. de Cuevas, 2002a: An ocean resonance in the southeast Pacific. *Geophys. Res. Lett.*, **29**, 1252, <https://doi.org/10.1029/2001GL014259>.
- , and —, 2002b: An ocean resonance in the Indian sector of the Southern Ocean. *Geophys. Res. Lett.*, **29**, 1664, <https://doi.org/10.1029/2002GL015270>.
- , and —, 2003: The region of large sea surface height variability in the southeast Pacific Ocean. *J. Phys. Oceanogr.*, **33**, 1044–1056, [https://doi.org/10.1175/1520-0485\(2003\)033<1044:TROLSS>2.0.CO;2](https://doi.org/10.1175/1520-0485(2003)033<1044:TROLSS>2.0.CO;2).
- Weijer, W., 2010: An almost-free barotropic mode in the Australian–Antarctic Basin. *Geophys. Res. Lett.*, **37**, L10602, <https://doi.org/10.1029/2010GL042657>.
- , S. T. Gille, and F. Vivier, 2009: Modal decay in the Australia–Antarctic basin. *J. Phys. Oceanogr.*, **39**, 2893–2909, <https://doi.org/10.1175/2009JPO4209.1>.
- Wiese, D. N., F. W. Landerer, and M. M. Watkins, 2016: Quantifying and reducing leakage errors in the JPL RL05M GRACE mascon solution. *Water Resour. Res.*, **52**, 7490–7502, <https://doi.org/10.1002/2016WR019344>.
- Willebrand, J., 1978: Temporal and spatial scales of the wind field over the North Pacific and North Atlantic. *J. Phys. Oceanogr.*, **8**, 1080–1094, [https://doi.org/10.1175/1520-0485\(1978\)008<1080:TASSOT>2.0.CO;2](https://doi.org/10.1175/1520-0485(1978)008<1080:TASSOT>2.0.CO;2).
- , S. G. H. Philander, and R. C. Pacanowski, 1980: The oceanic response to large-scale atmospheric disturbances. *J. Phys. Oceanogr.*, **10**, 411–429, [https://doi.org/10.1175/1520-0485\(1980\)010<0411:TORTLS>2.0.CO;2](https://doi.org/10.1175/1520-0485(1980)010<0411:TORTLS>2.0.CO;2).
- Wright, D. G., D. A. Greenberg, and F. G. Majaess, 1987: The influence of bays on adjusted sea level over adjacent shelves with application to the Labrador shelf. *J. Geophys. Res.*, **92**, 14 610–14 620, <https://doi.org/10.1029/JC092iC13p14610>.
- Wunsch, C., 1991: Large-scale response of the ocean to atmospheric forcing at low frequencies. *J. Geophys. Res.*, **96**, 15 083–15 092, <https://doi.org/10.1029/91JC01457>.
- , and D. Stammer, 1997: Atmospheric loading and the oceanic “inverted barometer” effect. *Rev. Geophys.*, **35**, 79–107, <https://doi.org/10.1029/96RG03037>.
- , and P. Heimbach, 2007: Practical global oceanic state estimation. *Physica D*, **230**, 197–208, <https://doi.org/10.1016/j.physd.2006.09.040>.
- , and —, 2013: Dynamically and kinematically consistent global ocean circulation and ice state estimates. *Ocean Circulation and Climate: A 21st Century Perspective*, International Geophysics Series, Vol. 103, Academic Press, 553–579, <https://doi.org/10.1016/B978-0-12-391851-2.00021-0>.